A Microscale View of Mixing and Overturning across the Antarctic Circumpolar Current

ALBERTO C. NAVEIRA GARABATO

University of Southampton, National Oceanography Centre, Southampton, United Kingdom

KURT L. POLZIN

Woods Hole Oceanographic Institution, Woods Hole, Massachusetts

RAFFAELE FERRARI

Massachusetts Institute of Technology, Cambridge, Massachusetts

JAN D. ZIKA AND ALEXANDER FORRYAN

University of Southampton, National Oceanography Centre, Southampton, United Kingdom

(Manuscript received 3 February 2015, in final form 27 October 2015)

ABSTRACT

The relative roles of isoneutral stirring by mesoscale eddies and dianeutral stirring by small-scale turbulence in setting the large-scale temperature–salinity relation of the Southern Ocean against the action of the overturning circulation are assessed by analyzing a set of shear and temperature microstructure measurements across Drake Passage in a "triple decomposition" framework. It is shown that a picture of mixing and overturning across a region of the Antarctic Circumpolar Current (ACC) may be constructed from a relatively modest number of microstructure profiles. The rates of isoneutral and dianeutral stirring are found to exhibit distinct, characteristic, and abrupt variations: most notably, a one to two orders of magnitude suppression of isoneutral stirring in the upper kilometer of the ACC frontal jets and an order of magnitude intensification of dianeutral stirring in the subpycnocline and deepest layers of the ACC. These variations balance an overturning circulation with meridional flows of $O(1)$ mm s^{-1} across the ACC's mean thermohaline structure. Isoneutral and dianeutral stirring play complementary roles in balancing the overturning, with isoneutral processes dominating in intermediate waters and the Upper Circumpolar Deep Water and dianeutral processes prevailing in lighter and denser layers.

1. Introduction

The meridional overturning circulation and stratification of the global ocean are shaped critically by processes in the Southern Ocean [see Marshall and Speer (2012) and Rintoul and Naveira Garabato (2013) for recent reviews]. The zonally unblocked nature of the Antarctic Circumpolar Current (ACC) system confers the region with a set of special dynamics that ultimately results in the focusing therein of large vertical exchanges between layers spanning the global ocean pycnocline. The nature of these exchanges has been the subject of an extensive body of theoretical and modeling work. Although the existence of an intricate coupling between zonal flow and meridional overturning in the ACC is unanimously highlighted by that literature, there is no consensus to date on the specific dynamical controls of the circulation.

Efforts to unravel the dynamics that regulate the extension of meridional overturning across the Southern Ocean and its associated hydrographic structure have regularly focused on understanding how the region is forced by wind and air–sea exchanges of buoyancy.

Corresponding author address: Alberto C. Naveira Garabato, University of Southampton, National Oceanography Centre, Southampton, SO14 3ZH United Kingdom.
E-mail: acng@noc.soton.ac.uk

DOI: 10.1175/JPO-D-15-0025.1

Appealing to residual-mean theory, the circulation ensuing from these forcings is conceptually expressed as an interplay between an Eulerian-mean, wind-driven Ekman overturning cell that acts to overturn isoneutral surfaces and a mesoscale eddy-induced cell that acts to flatten those surfaces. In this paradigm, the Southern Ocean overturning is portrayed to consist of upwelling of Circumpolar Deep Water (CDW) along poleward-shoaling isoneutrals, and isoneutral-following, northward downwelling of denser Antarctic Bottom Water (AABW) and of lighter Subantarctic Mode Water (SAMW) and Antarctic Intermediate Water (AAIW). Water mass transformations [defined here as transfers of water between adjacent potential temperature–salinity (θ–S) classes] are commonly assumed to be confined to the surface mixed layer. This assumption, however, appears at odds with the observation of widespread, significant, large-scale thermohaline gradients along interior isoneutral surfaces in the ACC (e.g., Zika et al. 2009) and with the wide recognition of the region as a hub of vigorous mesoscale eddy and internal wave motions [see Rintoul and Naveira Garabato (2013) and references therein], which are efficient stirrers along and across isoneutrals, respectively (Ferrari and Polzin 2005).

Motivated by this apparent inconsistency, in this article we sidestep the prevalent dynamical discussion and approach the problem from a different angle. We use measurements of the microscale signatures of isoneutral and dianeutral stirring along a section crossing the ACC to assess their relative contributions to balancing large-scale overturning. The theory of how turbulent flows propagate surface thermohaline forcing into the interior to establish the mean θ–S relationship of the ocean, which underpins our approach, is discussed in section 2. Our dataset and analysis techniques are outlined in section 3. Sections 4 and 5 present our quantification of mixing and overturning, respectively, across the ACC. Results are discussed in section 6, and our main findings are reviewed in section 7.

2. Theory

a. The mean θ–S relationship of the ocean

The mean θ–S relationship of the ocean is established by fluctuating flows acting on a wide range of spatial and temporal scales. This is often expressed by writing the conservation equation for the mean potential temperature $\overline{\theta}$ as

$$\partial_t\overline{\theta} + \overline{\mathbf{u}}\cdot\nabla\overline{\theta} = -\nabla\cdot(\overline{\mathbf{u}'\theta'} - \kappa\nabla\overline{\theta}), \tag{1}$$

where a "Reynolds decomposition" of variables into a slowly changing mean state (indicated by an overbar) and fluctuations (denoted by primes) has been adopted to allow investigation of the influence of the fluctuations on the mean. Here, $\mathbf{u}$ is the three-dimensional velocity vector, and κ is the molecular diffusivity of θ. The first term on the right-hand side represents the eddy flux. The second term is the dissipation of mean potential temperature gradients by molecular motions and may be generally neglected (Ferrari and Polzin 2005).

Following, for example, Ferrari et al. (2008), the eddy flux can be decomposed into diffusive and skew components by projecting it along and across the mean potential temperature gradient, and (1) can be rewritten as

$$\partial_t\overline{\theta} + \left(\overline{\mathbf{u}} + \nabla\times\frac{\overline{\mathbf{u}'\theta'}\times\nabla\overline{\theta}}{|\nabla\overline{\theta}|^2}\right)\cdot\nabla\overline{\theta} = -\nabla\cdot\left(\frac{\overline{\mathbf{u}'\theta'}\cdot\nabla\overline{\theta}}{|\nabla\overline{\theta}|^2}\nabla\overline{\theta}\right), \tag{2}$$

where the last term on the left-hand side and the first term on the right-hand side are the skew and diffusive components of the eddy flux, respectively, denoting fluxes along and across the mean gradient. Defining the residual-mean velocity as $\overline{\mathbf{u}}^\dagger = \overline{\mathbf{u}} + \nabla\times[(\overline{\mathbf{u}'\theta'}\times\nabla\overline{\theta})/|\nabla\overline{\theta}|^2]$ (Plumb and Ferrari 2005),[1] we obtain

$$\partial_t\overline{\theta} + \mathbf{u}^\dagger\cdot\nabla\overline{\theta} = -\nabla\cdot\left(\frac{\overline{\mathbf{u}'\theta'}\cdot\nabla\overline{\theta}}{|\nabla\overline{\theta}|^2}\nabla\overline{\theta}\right). \tag{3}$$

Equation (3) indicates that only the diffusive eddy flux can change the mean potential temperature following the residual mean flow, so this is the focus of the remainder of this section.

To relate the diffusive eddy flux to measurable quantities, we invoke the potential temperature variance equation:

$$\frac{\partial\overline{\theta'^2}}{\partial t} + \nabla\cdot(\overline{\mathbf{u}}\,\overline{\theta'^2} + \overline{\mathbf{u}'\theta'^2} - \kappa\nabla\overline{\theta'^2}) + 2\overline{\mathbf{u}'\theta'}\cdot\nabla\overline{\theta} = -2\kappa\overline{\nabla\theta'\cdot\nabla\theta'}, \tag{4}$$

which, assuming eddy fluctuations to be statistically stationary and homogeneous (such that the first four terms on the left-hand side vanish), may be reduced to

[1] Note that the definition of the residual-mean velocity is formally tracer dependent. Although here we adopt a definition in terms of θ, as appropriate to our analysis, we expect this residual-mean velocity to apply approximately to other climatically important tracers with regional distributions that are closely related to that of θ (e.g., S and biogeochemical tracers).

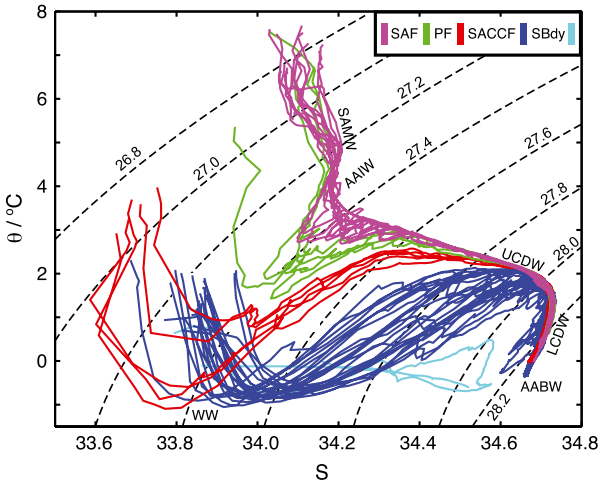

FIG. 1. θ–S diagram along the SR1b transect across Drake Passage in December 1997/January 1998. θ–S curves are colored according to the interfrontal zone in which they lie. Selected neutral density contours (computed as polynomial fits to the neutral density data of the Southern Ocean Database; see http://wocesoatlas.tamu.edu) are shown in black. Major water masses (AABW; AAIW; SAMW; UCDW/LCDW; WW) and fronts (PF; SACCF; SAF; SBdy = Southern Boundary) are labeled. The section location and characteristic frontal positions are indicated in Fig. 2. (Adapted from NG11.).

$$\overline{\mathbf{u}'\theta'}\cdot\nabla\overline{\theta} = -\kappa\overline{\nabla\theta'\cdot\nabla\theta'} = -\frac{1}{2}\chi, \tag{5}$$

where χ is the rate of dissipation of temperature variance, which can be measured with fast-response temperature probes. This is the Osborn–Cox relation (Osborn and Cox 1972) and states that the temperature variance generated by eddy fluctuations stirring the mean gradient is removed by molecular mixing. Note that only the diffusive component of the eddy temperature flux is involved in the generation of variance.

As discussed by Ferrari and Polzin (2005), the mean in the Osborn–Cox relation strictly includes all scales upon which microscale motions act, from the large, slowly evolving scales of the general circulation to the "intermediate" scales of mesoscale eddies and internal waves. The signatures of this collection of motions are plainly visible in the θ–S relationship characteristic of the ACC, illustrated by Fig. 1, which is based on CTD measurements across Drake Passage with a vertical resolution of $O(1)$ m. While small-scale turbulent overturns are not resolved in this dataset, the presence of at least two other classes of flows with distinct scales is suggested in the θ–S diagram: a large-scale background with vertical scales of $O(100$–$1000)$ m, which is laterally coherent on horizontal scales of $O(100)$ km, is largely stable on time scales of years to decades and is associated with the general circulation; and finescale structure with vertical scales of $O(10$–$100)$ m, which is laterally incoherent on horizontal scales of $O(1$–$10)$ km, is variable on time scales of days and is associated with intermediate-scale motions [primarily mesoscale eddies; see, e.g., Polzin and Ferrari (2004) and Naveira Garabato et al. (2011, hereinafter referred to as NG11)]. We refer the reader to appendix B of NG11 for an extensive discussion of the rationale for our interpretation of the thermohaline finestructure in the ACC as arising primarily from mesoscale eddy stirring.

To assess how the interplay between intermediate- and small-scale flows establishes the large-scale θ–S relationship of the ocean, it is insightful to recast the Osborn–Cox relation [(5)] in terms of a triple decomposition of variables into a large-scale mean, mesoscale fluctuations, and microscale turbulence (Joyce 1977; Davis 1994; Garrett 2001). As shown by Ferrari and Polzin (2005), this yields

$$\begin{aligned}\langle\mathbf{u}_e\theta_e\rangle\cdot\nabla_{\parallel}\theta_m + \langle\mathbf{u}_t\theta_t\rangle\cdot\nabla_{\perp}\theta_m \\ = -K_e|\nabla_{\parallel}\theta_m|^2 - K_t|\nabla_{\perp}\theta_m|^2 = -\frac{1}{2}\langle\chi\rangle,\end{aligned} \tag{6}$$

where the subscripts m, e, and t denote variables associated with the large-scale mean, mesoscale fluctuations, and microscale turbulence, respectively; angled brackets represent an average over a spatial scale large in comparison with that of the mesoscale fluctuations but small in relation to that of the large-scale mean; $\nabla_{\perp}$ and $\nabla_{\parallel}$ respectively refer to the gradient operators across and along neutral density surfaces; K_t and K_e are dianeutral and isoneutral diffusivities, respectively; and stationarity and homogeneity have been assumed. This expression states that the potential temperature variance generated by mesoscale eddy-induced isoneutral stirring (the first term on the left-hand side) and dianeutral stirring associated with small-scale turbulence (the second term on the left-hand side) acting on the large-scale mean state is dissipated by molecular mixing. We note that the balance between the generation of temperature variance by mesoscale eddy stirring and its dissipation by molecular mixing is not expected to hold on a local basis. Computations of tracer variance budgets in eddy-resolving numerical models (e.g., Wilson and Williams 2004; Abernathey and Marshall 2013) have routinely shown that the advection and triple correlation terms on the left-hand side of (4), which we have neglected in deriving (5)–(6), are significant over horizontal scales smaller than $O(100$–$500)$ km. Thus, we expect the balance in (6) to hold only when integrated over larger horizontal scales. In section 6, we will show that the assumption of (6)

produces physically plausible patterns of isoneutral stirring and argue that this positive result stems from the persistence of thermohaline variance over horizontal scales of $O(1000)$ km in the ACC.

Equation (6) may be used to estimate K_e by exploiting the relation between K_t and the rate of dissipation of turbulent kinetic energy ϵ, which can be readily computed from shear microstructure measurements (Osborn and Cox 1972). This relation is given by

$$K_t = \frac{\Gamma \epsilon}{N^2}, \tag{7}$$

where Γ is a mixing efficiency [take to be 0.2, as relevant to shear-driven turbulence (Osborn 1980)], and N is the buoyancy frequency. This yields the expression

$$K_e = \frac{\langle \chi \rangle / 2 - \Gamma N^{-2} \epsilon |\nabla_\perp \theta_m|^2}{|\nabla_\parallel \theta_m|^2}, \tag{8}$$

with which K_e may be determined from microstructure measurements of ϵ and χ and knowledge of the large-scale potential temperature and density fields. In this way, the relative contributions of intermediate- and small-scale flows to the establishment of the mean θ–S relationship of the ocean are assessed. Note that the dianeutral production of temperature variance by double-diffusive instabilities is not represented explicitly in (8), on the basis of preceding arguments on its likely insignificance at leading order (see NG11 and references therein). Any generation of variance by these processes will be amalgamated into the isoneutral production term and so will bias K_e high.

In the absence of microstructure observations, an alternative approach to the estimation of K_e has been used in the past, founded on the measurement of thermohaline finestructure. This relies on the formulation of the downgradient transport of a scalar tracer (e.g., θ) as

$$\left(\frac{\overline{\mathbf{u}'\theta'} \cdot \nabla \overline{\theta}}{|\nabla \overline{\theta}|^2} \nabla \overline{\theta} \right) = c_e L_{\text{mix}} U_{\text{rms}} |\nabla_\parallel \overline{\theta}| = K_e^{\text{fine}} |\nabla_\parallel \overline{\theta}|, \tag{10}$$

where

$$K_e^{\text{fine}} = c_e U_{\text{rms}} L_{\text{mix}} \tag{11}$$

is the finestructure-based estimate of K_e. Using observations, c_e has been estimated as ~0.16 from the analysis of a quasi-global inventory of moored current meter and temperature records (Wunsch 1999); U_{rms} may be readily computed as the one standard deviation in time of the eddy velocity directed across the time-mean flow (NG11); and L_{mix} can be calculated by applying the above definition in terms of θ_{rms} and $|\nabla_\parallel \overline{\theta}|$ to thermohaline finestructure-based estimates of these variables (see section 3b and NG11 for a discussion of the pertinent methodology).

Expression (10) is formally valid to the extent that potential temperature fluctuations are generated by local stirring of the large-scale gradient (i.e., advection of potential temperature variance from regions upstream is assumed to be negligible) and insofar as $|\nabla_\parallel \theta_m|$ varies slowly over the eddy mixing length L_{mix} (i.e., a scale separation between eddy and mean flow scales is assumed). The applicability of this local balance assumption to the ACC will be discussed in section 6.

b. *The overturning circulation across the ACC*

Knowledge of the distribution of the isoneutral and dianeutral turbulent diffusivities in the meridional–vertical plane (estimated as discussed in section 2a) may be used to quantitatively assess the overturning circulation across the ACC. To illustrate this point, consider the equation of conservation of mean potential temperature [(3)] in the limits of stationarity ($\partial_t \overline{\theta} \approx 0$) and negligibility of the zonal (strictly, along stream) advection of mean potential temperature by the residual mean flow ($\overline{u}^\dagger \partial_x \overline{\theta} \ll \overline{v}^\dagger \partial_y \overline{\theta} + \overline{w}^\dagger \partial_z \overline{\theta}$, as appropriate for a parallel shear flow):

$$\overline{v}^\dagger \partial_y \overline{\theta} + \overline{w}^\dagger \partial_z \overline{\theta} = \overline{v}_\parallel^\dagger \partial_\parallel \overline{\theta} + \overline{w}_\perp^\dagger \partial_\perp \overline{\theta} = -\nabla \cdot \left(\frac{\overline{\mathbf{u}'\theta'} \cdot \nabla \overline{\theta}}{|\nabla \overline{\theta}|^2} \nabla \overline{\theta} \right), \tag{12}$$

where $\overline{v}_\parallel^\dagger$ and $\partial_\parallel$ are the meridional components of the residual-mean velocity and the gradient operator directed along isoneutrals, and $\overline{w}_\perp^\dagger$ and $\partial_\perp$ are the dianeutral components of the residual-mean velocity and the gradient operator. An approximate alignment of the flow with isoneutral surfaces is regularly assumed in theoretical characterizations of cross-ACC overturning,

and $\overline{v}^{\dagger}_{\parallel}$ forms the basis of most common metrics of that circulation [see Marshall and Speer (2012) and references therein]. We caution that the neglect of residual-mean zonal advection of mean potential temperature in the derivation of (12) is of dubious local validity, particularly in dynamically active sectors of the ACC (Wilson and Williams 2004; Abernathey and Marshall 2013), where the mean flow configuration often deviates from a parallel shear flow. As such, our application of (12) represents a specific interpretation of the regional overturning circulation implied by the large-scale patterns of stirring in our dataset, rather than a rigorous assessment of the actual overturning. In section 5, we will show that applying (12) to our data yields an overturning circulation of physically plausible structure and magnitude, from which we surmise a posteriori that the exercise has scientific value.

Expression (12) is equivalent to the tracer contour equation of Zika et al. (2010) and states that, under the aforementioned approximations, the residual mean flow across mean potential temperature contours must be balanced by the divergence of the (isoneutral and dianeutral) turbulent potential temperature fluxes. Using (5)–(6), (12) may be expressed as

$$\overline{v}^{\dagger}_{\parallel}\partial_{\parallel}\theta_m + \overline{w}^{\dagger}_{\perp}\partial_{\perp}\theta_m = \partial_{\parallel}(K_e\partial_{\parallel}\theta_m) + \partial_{\perp}(K_t\partial_{\perp}\theta_m), \qquad (13)$$

where the approximation $\overline{\theta} \approx \theta_m$ has been adopted. This yields a definition for the meridional–isoneutral flow as

$$\overline{v}^{\dagger}_{\parallel} \approx (\partial_{\parallel}\theta_m)^{-1}[\partial_{\parallel}(K_e\partial_{\parallel}\theta_m) + \partial_{\perp}(K_t\partial_{\perp}\theta_m) - \overline{w}^{\dagger}_{\perp}\partial_{\perp}\theta_m]. \qquad (14)$$

The last term in (14) represents the component of meridional–isoneutral flow balanced by dianeutral flow across mean potential temperature contours and is zero in the limits of no dianeutral flow ($\overline{w}^{\dagger}_{\perp} = 0$) or a perpendicular arrangement of isothermal and isoneutral surfaces ($\partial_{\perp}\overline{\theta} = 0$). Assuming negligible nonlinearity in the equation of state (Klocker and McDougall 2010), $\overline{w}^{\dagger}_{\perp}$ may be related to ϵ by

$$\overline{w}^{\dagger}_{\perp} \approx \Gamma N^{-2}\partial_{\perp}\epsilon. \qquad (15)$$

The set of relations (7)–(8) and (14)–(15) underpins the characterization of mixing and overturning across the ACC from microstructure observations carried out in this study.

3. Data and analysis

a. Data

The data analyzed here consist of hydrographic, velocity, and microstructure measurements collected during three repeats of the SR1b section across the eastern Drake Passage (Fig. 2), under the auspices of the Diapycnal and Isopycnal Mixing Experiment in the Southern Ocean [DIMES; see Sheen et al. (2013) and references therein]. The SR1b section crosses the two major ACC jets in the region, associated with the Subantarctic Front (SAF) and Polar Front (PF). The details of each of the section occupations considered in this study are provided by Table 1.

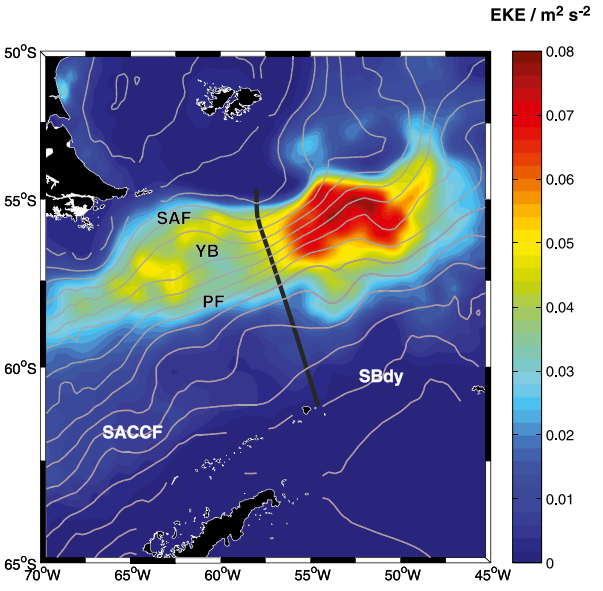

FIG. 2. Position of the SR1b repeat section (in black). Surface eddy kinetic energy calculated from the AVISO gridded altimetry product for 1992–2011 is shown in color. Mean dynamic topography contours at intervals of 0.1 m are indicated in gray (Maximenko et al. 2009). Characteristic frontal positions are marked, with labels defined in Fig. 1. YB denotes the Yaghan basin.

Profiles of temperature, salinity, and pressure were obtained with a SeaBird 911 Plus CTD at an effective vertical resolution of $O(1)$ m. The accuracy of temperature measurements was 0.001°C, and that of the salinity measurements was 0.002 after calibration by reference to bottle salinity samples analyzed on a Guildline 8400B salinometer using the International Association for the Physical Sciences of the Oceans (IAPSO) P-series standard seawater. Profiles of horizontal velocity were obtained with a downward-looking 300-kHz Teledyne RDI lowered acoustic Doppler current profiler (LADCP) mounted on the CTD frame and programmed to obtain beam-coordinate velocities in 8-m bins. The LADCP data were processed using the velocity-inversion method of Visbeck (2002), of which the velocity referencing stage was accomplished with bottom-track LADCP, shipboard ADCP, and vessel global positioning system data. Further details on the CTD and LADCP data acquisition and

TABLE 1. SR1b repeat section occupations analyzed in this study. The cruise code, vessel, and dates of and data collected in each occupation are listed. RRS stands for Royal Research Ship.

Cruise code	Vessel	Dates of occupation	Data
JR0a	RRS James Clark Ross	21–26 Nov 1993	30 CTD stations
JR0b	RRS James Clark Ross	15–21 Nov 1994	27 CTD stations
JR16	RRS James Clark Ross	15–20 Nov 1996	29 CTD stations
JR27	RRS James Clark Ross	29 Dec 1997–7 Jan 1998	50 CTD stations
JR47	RRS James Clark Ross	22–28 Nov 2000	30 CTD stations
JR67	RRS James Clark Ross	20–26 Nov 2001	30 CTD stations
JR81	RRS James Clark Ross	27 Dec 2002–1 Jan 2003	30 CTD stations
JR94	RRS James Clark Ross	11–15 Dec 2003	30 CTD stations
JR115	RRS James Clark Ross	2–8 Dec 2004	30 CTD stations
JR139	RRS James Clark Ross	7–12 Dec 2005	30 CTD stations
JR276	RRS James Clark Ross	13–25 Apr 2011	14 CTD stations, 13 VMP-5500 stations
JC69	RRS James Cook	7–12 Mar 2012	16 CTD stations, 14 VMP-5500 stations
JR281	RRS James Clark Ross	19–27 Mar 2013	30 CTD stations, 12 VMP-5500 stations

processing are provided in the cruise reports (Watson 2011, 2012; Sallée 2013).

Full-depth measurements of ϵ and χ were obtained using two Rockland Scientific International free-falling VMP-5500 vertical microstructure profilers (http://www.rocklandscientific.com) operated by the National Oceanography Centre, Southampton, and the Woods Hole Oceanographic Institution. One of the instruments was deployed at most CTD stations along each SR1b section occupation and recorded vertical gradients in velocity and temperature on centimeter scales (from which ϵ and χ were respectively computed) at 512 Hz to within 100 m of the ocean floor. Data processing was conducted using algorithms developed originally for the High Resolution Profiler (Polzin and Montgomery 1996; Naveira Garabato 2009). Variances of the vertical gradients in velocity and temperature were calculated every 0.5 dbar, using bin widths of 1 s. Each VMP-5500 carried two shear probes and two fast-response thermistors, and unless one sensor of each pair was deemed noisy, the mean of the ϵ or χ estimates from each sensor pair was used. Values of ϵ were computed from the vertical shear variance $(\partial u/\partial z)^2$ as $\epsilon = (15/2)\nu(\partial u/\partial z)^2$ (Oakey 1982), where ν is the molecular viscosity and isotropy is assumed. Values of χ were calculated from the variance of the vertical temperature gradient $(\partial\theta/\partial z)^2$ as $\chi = 6\kappa(\partial\theta/\partial z)^2$ (Oakey 1982), where the assumption of isotropy is adopted again. Prior to the computation of χ, $(\partial\theta/\partial z)^2$ was corrected for nonlinearity and pressure dependence in the thermistors' response by reference to the temperature measurements obtained with a SeaBird 03F/04C CTD mounted on each VMP-5500 profiler. Microstructure cast locations were recorded as the midpoint between the instrument deployment and recovery positions, profiler drift being rarely more than a few kilometers.

b. Analysis

The rates of mixing and overturning across the ACC are estimated from microstructure observations by applying the set of relations (7)–(8) and (14)–(15) to individual SR1b transect occupations. For each station in each section repeat, measurements of ϵ and χ are bin averaged in neutral density γ^n (Jackett and McDougall 1997) bins of 0.08 kg m^{-3}, and N^2 is computed in the same bins from the CTD data. The selected bin size represents a compromise between the vertical resolution and statistical robustness of the bin-averaged microstructure variables, but our results are qualitatively insensitive to this choice. To define the large-scale mean potential temperature θ_m along a given transect occupation, the CTD measurements of θ for that section repeat are bin averaged in the same density intervals, and a cubic spline is fitted to the binned θ values on each isoneutral surface (as in NG11). The resulting θ_m field contains all the large-scale features of the original potential temperature distribution, where large-scale here refers to structures that span several stations in the horizontal and several density bins in the vertical. All isoneutral and dianeutral gradients are computed using centered differencing in along-section distance–neutral density space, except for the northernmost and southernmost stations in each section occupation and for density bins adjacent to bins with absent data, for which forward or backward differencing is used. Before displaying the (isoneutral and dianeutral) turbulent potential temperature fluxes in (14) and computing their divergences, the K_e and K_t fields are smoothed with a 2D boxcar filter of width equal to double the station spacing in along-section distance and to double the bin size in γ^n. This exercise brings out the large-scale patterns in the turbulent potential temperature fluxes but does not significantly affect our estimates of $\overline{v}^{\dagger}_{\|}$. The uncertainties in bin-averaged ϵ, χ, θ_m, and all other derived

variables are estimated as explained in the appendix, section a, and displayed in all figures where clarity permits.

An alternative estimation of K_e is conducted by applying expression (11) to observations of thermohaline finestructure. We follow the methodology outlined by NG11, in which $\overline{\theta}$ and $\theta_{\rm rms}$ are respectively estimated as a set of cubic spline fits to the measured large-scale potential temperature distribution along individual isoneutral surfaces and as the rms value of the observed deviations from those fits. We update their calculation for the SR1b transect by adding the CTD data from the three recent occupations at the core of the present study to their set of 10 historical section repeats (Table 1). We note that results from the analysis of this expanded dataset are very similar to those of calculations based solely on the section repeats of NG11 or on the three recent occupations. As discussed by those authors, the statistical robustness of the analysis is much improved by considering a large number of section repeats, so only results related to the expanded dataset are discussed in the present work. To compare $K_e^{\rm fine}$ estimates, which are computed in a reference frame that has dynamic height as the horizontal coordinate (NG11), with microstructure-based estimates of K_e, which are calculated in a geographic reference frame, we linearly interpolate the $K_e^{\rm fine}$ field to the dynamic height of each of the three recent section repeats.

4. Mixing across the ACC

Our calculation of the rates of dianeutral and isoneutral stirring across the ACC from microstructure observations is illustrated here by the analysis of the JC69 cruise data (Table 1). This section occupation had somewhat more regular sampling than the other two SR1b repeat microstructure transects and yields very similar results to an analysis of those transects. An overview of the hydrographic and flow structure of the ACC in the JC69 occupation is given by Figs. 3a–c, which respectively show the measured distributions of θ, N^2, and flow speed with isoneutrals overlaid. The slope of the southward-shoaling isoneutrals of the ACC is punctuated by two clear inflections associated with the flow speed maxima of the SAF and PF jets. While θ and N^2 are relatively homogeneous along isoneutrals below the surface mixed layer, significant isoneutral gradients in both variables occur concurrently in the uppermost ~1 km of the fronts, particularly in the transition between Winter Water (WW) and AAIW and at the poleward edge of SAMW. Note that a reversal in isoneutral slopes and water mass properties occurs in the two southernmost stations of the section, suggesting that these sampled a transient mesoscale meander of the PF.

Microstructure estimates of ϵ and χ along the same repeat transect are presented in Figs. 3d and 3e, respectively. The two variables exhibit a broadly similar distribution, suggesting that dianeutral stirring is likely to play an important role in balancing the dissipation of temperature variance across much of the section. Elevated values (approaching or exceeding $10^{-9}\,{\rm W\,kg^{-1}}$ in ϵ and $10^{-9}\,{\rm °C^2\,s^{-1}}$ in χ) are generally found in the uppermost ~1 km of the water column and in the deepest ~1 km in areas of complex topography and beneath the ACC frontal jets. As discussed in section 6, the intensification of turbulent dissipation in the upper ocean occurs primarily in association with wind-generated near-inertial waves, and elevated dissipation at depth is linked to internal waves radiated as the deep ACC eddy flows impinge on rough topography. However, there are also instances of qualitative disagreement between ϵ and χ below the base of the main pycnocline at ~150 m (most clearly, in the group of isoneutrals connecting WW with AAIW), where elevated dissipation of temperature variance coincides with modest turbulent dissipation. This discrepancy hints at the local dominance of isoneutral stirring in balancing the dissipation of temperature variance.

To formally assess the relative contributions of dianeutral and isoneutral stirring to the temperature variance budget, the large-scale mean potential temperature θ_m is estimated, and the above measurements are reexamined in neutral density space (Fig. 4). The alignment of the steepest isoneutral slopes and the sharpest isoneutral gradients in θ_m (Figs. 4a,b) and in N^2 (Fig. 4d) with the flow speed maxima of the SAF and PF jets (Fig. 4e) can be readily appreciated. The dianeutral gradient in θ_m (Fig. 4c) is most pronounced in the uppermost ~500 m throughout the section, particularly around the WW layer at and south of the PF. The broad similarity between the distributions of ϵ (Fig. 4f) and χ (Fig. 4h) and the increase of both variables in the upper ocean and near the seafloor are again apparent, as is, more subtly, the general qualitative enhancement of χ over ϵ between approximately 150 and 1000 m. While this last feature is suggestive of the significance of isoneutral stirring in that depth range, there is no obvious intensification of χ at fronts (i.e., where $|\partial_{\|}\theta_m|$ is largest), as might have been expected if the rate of isoneutral stirring was invariable across the ACC.

Combining N^2 (Fig. 4e) and ϵ (Fig. 4f) in (7), an estimate of the dianeutral turbulent diffusivity K_t is obtained (Fig. 4h). Elevated values of K_t approaching $10^{-4}\,{\rm m^2\,s^{-1}}$ are common near the sea surface and in the vicinity of the ACC jets at depths exceeding ~1000 m, whereas diffusivities that are smaller by one order of magnitude are characteristic of the intervening depth

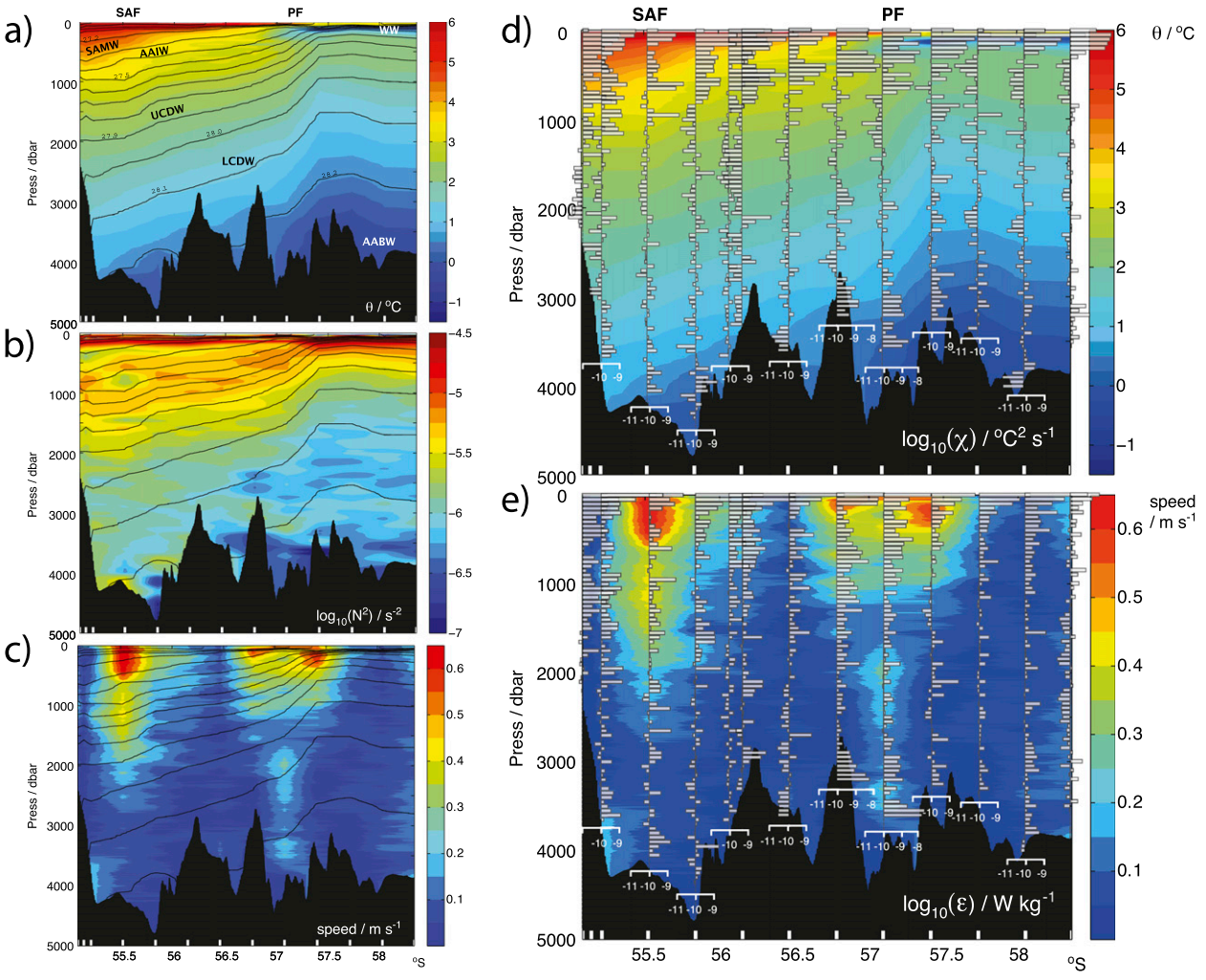

FIG. 3. Meridional sections along the JC69 occupation of the SR1b transect of (a) θ, (b) N^2, and (c) LADCP-measured speed, in color, and (d) χ and (e) ϵ, indicated by bars. Neutral density contours are superimposed on (a)–(c) and labeled in (a). Major water masses are marked in (a) and labeled as in Fig. 1. Frontal positions are indicated in the upper axis. For reference, θ and speed are shown by the background shading in (d) and (e), respectively.

range. See Sheen et al. (2013, 2014) for a detailed discussion of the distribution and physical controls of K_t along the SR1b section.

A direct comparison between the rate of dissipation of temperature variance $\chi/2$ and the rate of production by dianeutral stirring $K_t|\partial_\perp\theta_m|^2$ in (6) is shown in Fig. 5. Confirming the qualitative impression garnered from Figs. 3d–e and 4f–h, section-mean profiles (Fig. 5a, left) indicate that dianeutral production generally balances (within uncertainties) the measured dissipation of temperature variance in density classes lighter than $27.2\,\mathrm{kg\,m^{-3}}$ or denser than $27.9\,\mathrm{kg\,m^{-3}}$. Elsewhere, there is typically a half to two orders of magnitude deficit in dianeutral production that must be offset by isoneutral production. As found by Ferrari and Polzin (2005) in the subtropical Northeast Atlantic, the range of density classes in which isoneutral production is significant is characterized by enhanced θ–S variability along isoneutrals (Fig. 5a, middle).

A decomposition of the section-mean profiles of the rates of dissipation and dianeutral production of temperature variance into areas between and within fronts (Fig. 5b) reveals that the importance of isoneutral production in intermediate density classes pertains primarily to frontal regions. Outside the fronts, there is a near-ubiquitous balance between dissipation and dianeutral production. This general pattern is also apparent in the station-by-station comparison conducted in Fig. 6a, where $\chi/2$ and $K_t|\partial_\perp\theta_m|^2$ are displayed against the backdrop of the θ_m field. There, it is seen that the imbalance between dissipation and dianeutral production peaks in the approximate 150–1000-m depth

range, affecting different groups of isoneutrals equatorward ($27.2 < \gamma^n < 27.5\,\mathrm{kg\,m^{-3}}$) and poleward ($27.7 < \gamma^n < 27.9\,\mathrm{kg\,m^{-3}}$) of the PF. This is consistent with thermohaline variance being produced along those density surfaces by isoneutral stirring at the PF (for the former density class) and at the Southern ACC Front (SACCF; for the latter density class), where those isoneutrals outcrop into the 100–200-m-deep remnant winter mixed layer (NG11).

Substituting the rates of dissipation and dianeutral production of temperature variance and $|\partial_\parallel \theta_m|$, in (8), an estimate of the isoneutral turbulent diffusivity K_e required for isoneutral production to balance the temperature variance budget may be obtained (Fig. 6b). The diffusivity K_e exhibits values spanning at least two orders of magnitude between $O(10)$ and $O(10^3$–$10^4)\,\mathrm{m^2\,s^{-1}}$. The most striking characteristic of the K_e distribution is its inverse relationship with flow speed: small diffusivities of $O(10$–$10^2)\,\mathrm{m^2\,s^{-1}}$ are found at the high-speed cores of the ACC frontal jets, typically at depths shallower than ~1000 m, and elevated diffusivities of $O(10^3)\,\mathrm{m^2\,s^{-1}}$ occur between and below the ACC frontal jet cores. As discussed in section 6, this result, obtained here from the centimeter-scale structure of velocity and temperature profiles across the ACC, resonates with the findings of several recent, largely theory- and model-grounded studies suggesting that mesoscale eddy stirring is regularly suppressed by the mean flow in the Southern Ocean (e.g., Smith and Marshall 2009; Ferrari and Nikurashin 2010, hereinafter referred to as FN10; Lu and Speer 2010; Abernathey et al. 2010; NG11; Sallée et al. 2011; Thompson and Sallée 2012; Klocker and Abernathey 2014). Of those, the mixing length theory-based analysis of thermohaline finestructure measurements of NG11 is the only study grounded on in situ hydrographic observations and is thus closely related to the present work. A comparison between our results and those authors' is undertaken in section 6.

5. Overturning circulation across the ACC

If the thermohaline structure of the ACC is to remain in an approximately stationary state in the presence of the distributions of (isoneutral and dianeutral) turbulent stirring diagnosed above (Figs. 6b and 4h, respectively), a cross-ACC overturning circulation must exist. In the limit represented by (14), this circulation is associated with an isoneutral advection of mean potential temperature $\overline{v}^\dagger_\parallel \partial_\parallel \theta_m$ that must be balanced by an isoneutral divergence of the isoneutral turbulent potential temperature flux $\partial_\parallel (K_e \partial_\parallel \theta_m)$; a dianeutral divergence of the dianeutral turbulent potential temperature flux $\partial_\perp (K_t \partial_\perp \theta_m)$; or a dianeutral advection of mean potential temperature $\overline{w}^\dagger_\perp \partial_\perp \theta_m$. Determination of this balance thus provides an estimate of the overturning circulation in the region of the measurements and permits a quantitative assessment of the physical processes balancing the circulation to be made. In this section, we first consider the contributions of the three terms on the right-hand side of (14) to balancing $\overline{v}^\dagger$ and then combine them to estimate the net meridional–isoneutral flow across our study area.

As outlined in section 2b, we caution that this exercise represents a specific interpretation of the regional overturning circulation implied by the observed patterns of stirring. It is not a rigorous assessment of the actual overturning because we lack prior knowledge of the extent to which the assumptions made in deriving (14) hold in our study area and of the degree of undersampling of the key stirring patterns in our dataset. To minimize the influence of these limitations, which is likely to be exacerbated at the spatial scales of the ACC jets (e.g., Abernathey and Marshall 2013), we estimate section-characteristic profiles of all terms on the right-hand side of (14) by focusing on the largest horizontal and vertical scales captured by our measurements. As this approach yields a physically plausible overturning circulation, we deduce that (14) provides a reasonable description of the ACC-wide balance between stirring and overturning in our study region.

The distribution of the isoneutral potential temperature flux entering the first term on the right-hand side of (14) for the JC69 data is shown in Fig. 7a. As might be expected from the stochasticity of the measured microscale variables and the "snapshot" character of the observations, $K_e \partial_\parallel \theta_m$ displays some noiselike variability between contiguous stations and isoneutral layers. However, it also exhibits significant large-scale structure. At and to the north of the PF, $K_e \partial_\parallel \theta_m$ is positive and increases northward in the approximate $27.2 < \gamma^n < 27.5\,\mathrm{kg\,m^{-3}}$ range, from $O(10^{-4})\,^\circ\mathrm{C\,m\,s^{-1}}$ within the PF to values up to one order of magnitude larger farther north. In contrast, at densities exceeding $27.6\,\mathrm{kg\,m^{-3}}$, $K_e \partial_\parallel \theta_m$ increases southward, from negative or small [generally of $O(10^{-4})\,^\circ\mathrm{C\,m\,s^{-1}}$ or less] positive fluxes north of the PF to positive values one order of magnitude greater at the PF. Given a generally positive isoneutral gradient in θ_m (Fig. 4b), (14) implies the occurrence of northward flow in the $27.2 < \gamma^n < 27.5\,\mathrm{kg\,m^{-3}}$ class and southward flow in denser layers, balanced by eddy-induced isoneutral stirring. The magnitude of these flows is estimated below. Note that the patterns of $K_e \partial_\parallel \theta_m$ and the implied sense of overturning reverse in the two southernmost stations, which are associated with a transient mesoscale feature (section 4) and are therefore excluded from the following calculation.

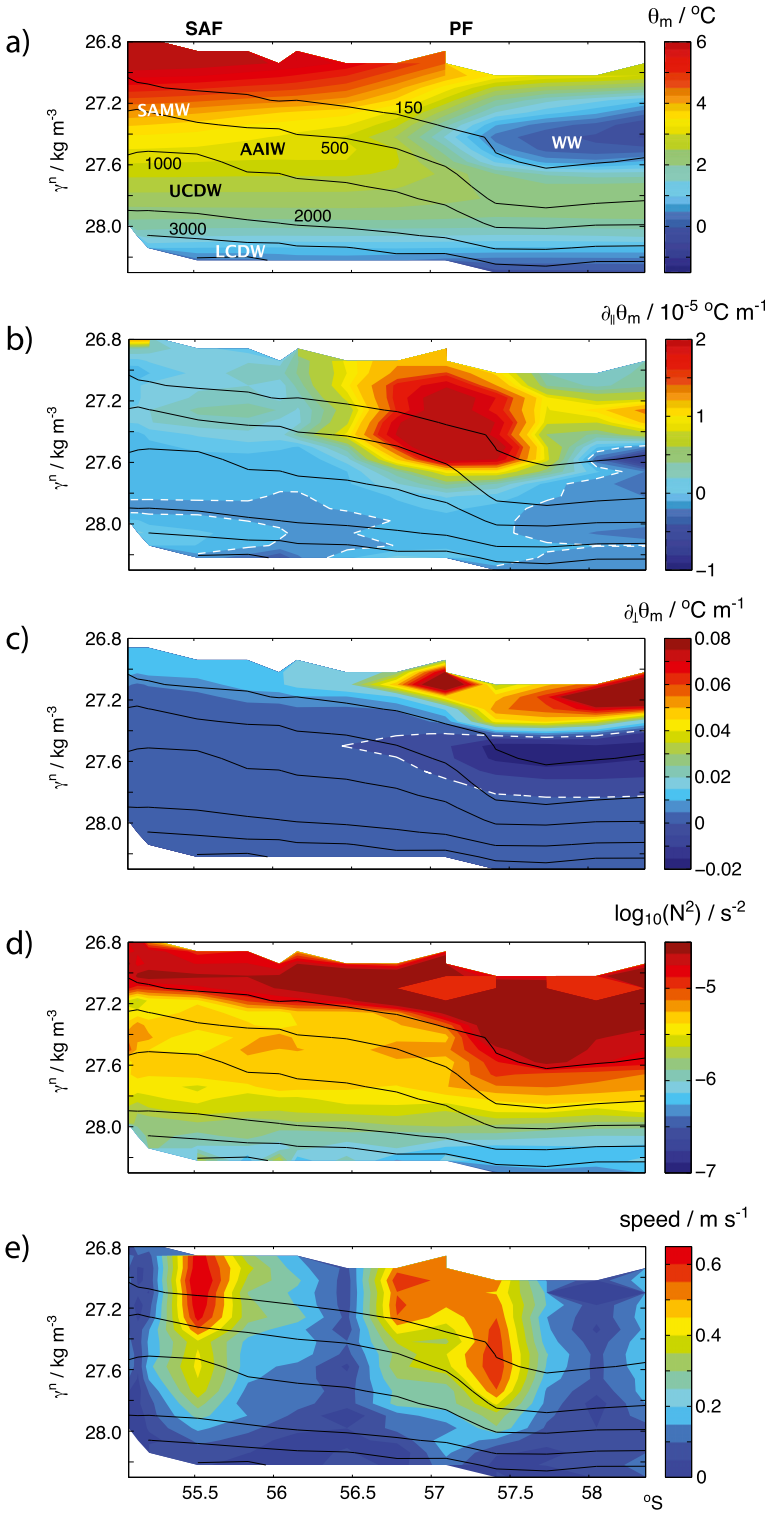

FIG. 4. Meridional sections along the JC69 occupation of the SR1b transect of (a) θ_m, (b) $\partial_{\|}\theta_m$, (c) $\partial_{\perp}\theta_m$, (d) N^2, and (e) LADCP-measured speed, in color, and (f) χ, (g) ϵ, and (h) K_t, indicated by bars. Pressure contours are superimposed on all panels and labeled in (a). Major water masses are marked in (a) and labeled as in Fig. 1. The zero contour is denoted by the white dashed lines in (b)–(c). Frontal positions are indicated in the upper axis. For reference, θ_m is shown by the background shading in (f) and speed in (g)–(h).

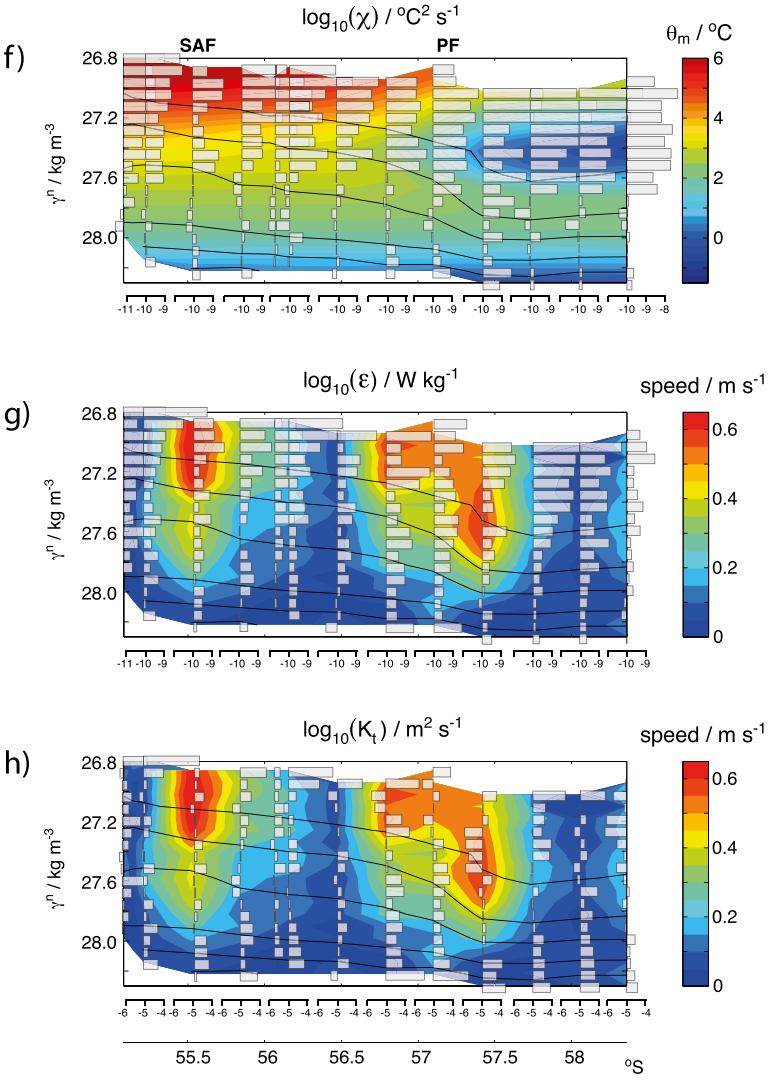

FIG. 4. (*Continued*)

To estimate the contribution of mesoscale eddy stirring to balancing meridional overturning in a manner that is robust to grid-scale variability and uncertainty in K_e and θ_m, we calculate section-characteristic vertical profiles of $\partial_\parallel(K_e\partial_\parallel\theta_m)$ and $\partial_\parallel\theta_m$. We do this by conducting a least squares linear fit to the distributions of $K_e\partial_\parallel\theta_m$ and θ_m along the section in each isoneutral layer, as illustrated by Fig. 7b, and computing the gradients of the fits. The ensuing profiles of $\partial_\parallel(K_e\partial_\parallel\theta_m)$ and $\partial_\parallel\theta_m$ are shown in Fig. 7c. The same features that were qualitatively appreciated in the transectwide distributions of both variables (Figs. 7a, 4b) are quantitatively reflected in the vertical profiles. The term $\partial_\parallel(K_e\partial_\parallel\theta_m)$ is positive in the approximate $27.2 < \gamma^n < 27.5\,\mathrm{kg\,m^{-3}}$ range, peaking at $5.2 \times 10^{-9}\,^\circ\mathrm{C\,s^{-1}}$ on the $\gamma^n = 27.34\,\mathrm{kg\,m^{-3}}$ surface and is negative in the $27.5 < \gamma^n < 28.0\,\mathrm{kg\,m^{-3}}$ class, with values of $O(-1 \times 10^{-9})\,^\circ\mathrm{C\,s^{-1}}$. Outside the $27.5 < \gamma^n < 28.0\,\mathrm{kg\,m^{-3}}$ range, $\partial_\parallel(K_e\partial_\parallel\theta_m)$ is not significantly different from zero. The term $\partial_\parallel\theta_m$ is positive throughout the water column. Taking the ratio of $\partial_\parallel(K_e\partial_\parallel\theta_m)$ to $\partial_\parallel\theta_m$, we obtain an estimate of the section-characteristic vertical profile of the meridional–isoneutral velocity $\overline{v}^\dagger_\parallel$ balanced by eddy stirring (Fig. 7c). The sense of the circulation is dictated by the sign of $\partial_\parallel(K_e\partial_\parallel\theta_m)$. Significant northward flow at a rate of up to $0.5\,\mathrm{mm\,s^{-1}}$ is surmised to occur in the $27.2 < \gamma^n < 27.5\,\mathrm{kg\,m^{-3}}$ range, and comparable southward flow is implied in the $27.5 < \gamma^n < 28.0\,\mathrm{kg\,m^{-3}}$ class. Southward flow is also suggested at densities lighter than $\gamma^n = 27.2\,\mathrm{kg\,m^{-3}}$, although its significance is marginal.

Next, we examine the distribution of the dianeutral potential temperature flux entering the second term on the right-hand side of (14) for the JC69 data, shown in Fig. 8a. There is a clear tendency for $K_t\partial_\perp\theta_m$ to increase from a

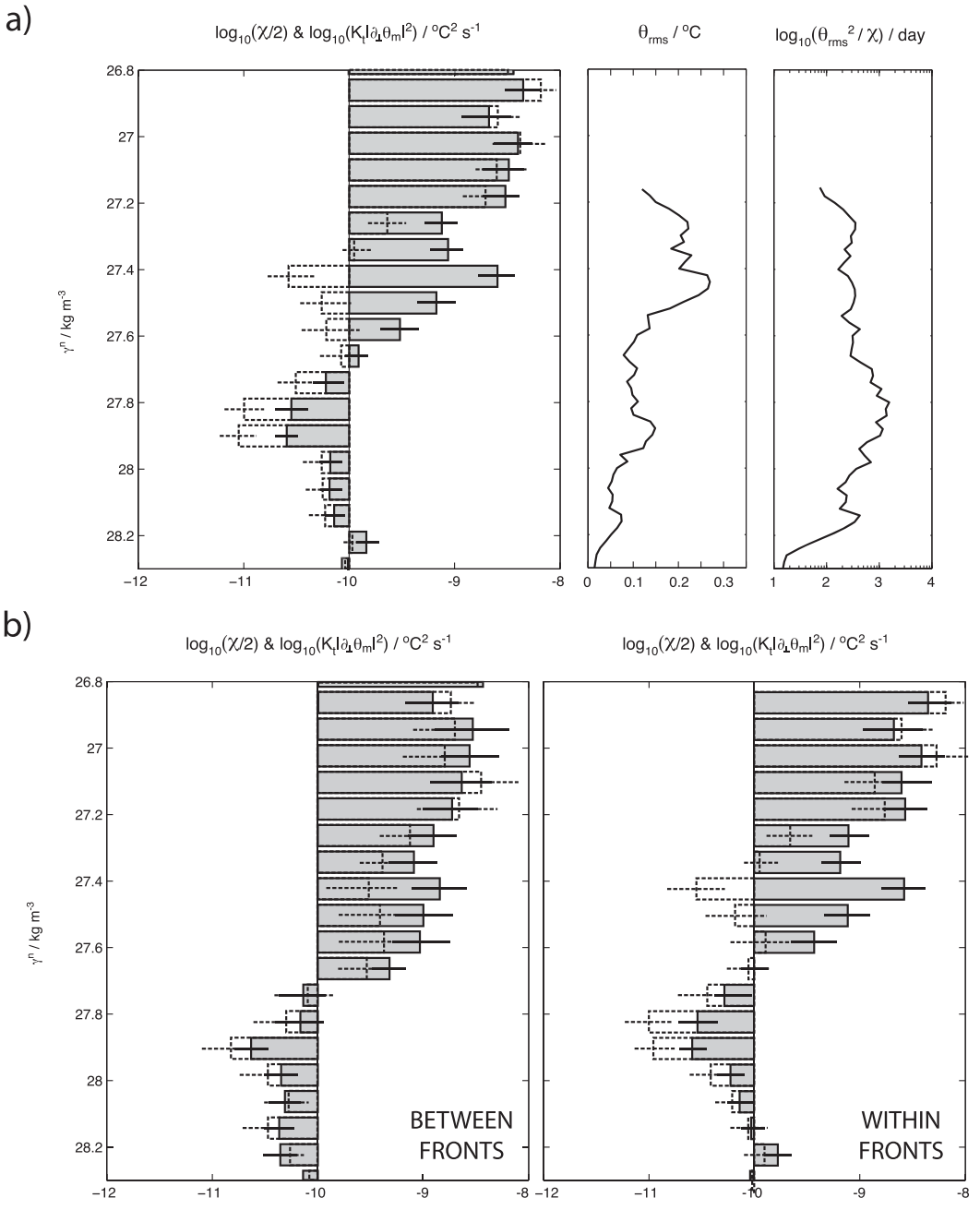

FIG. 5. (a) Mean profiles of (left) the rate of dissipation of temperature variance $\chi/2$ (gray bars) and the rate of dianeutral production of temperature variance $K_t|\partial_\perp\theta_m|^2$ (dashed bars), with uncertainties, for the JC69 occupation of the SR1b transect; (center) the rms potential temperature fluctuation in (10), estimated from all available SR1b hydrographic section repeats; and (right) the time scale of temperature variance dissipation, estimated as $\theta^2_{\rm rms}/\chi$ using the data in the left and center panels. (b) As in (a), but partitioned into stations (left) between frontal jets and (right) within frontal jets; a station is defined to be within a frontal jet if the LADCP-measured speed exceeds $0.15\,{\rm m\,s^{-1}}$ somewhere in the water column.

[small positive, of $O(10^{-8})$ °C m s^{-1}, or negative] minimum at depths around 500–1000 m to positive values typically one order of magnitude greater [i.e., of $O(10^{-7})$ °C m s^{-1}] in the upper ocean above 500 m and in the deep ocean below 1000 m. Considering the positive isoneutral gradient in θ_m, (14) indicates that this $K_t\partial_\perp\theta_m$ distribution is conducive to northward flow in the upper layers and to southward flow at depth, balanced by small-scale dianeutral stirring.

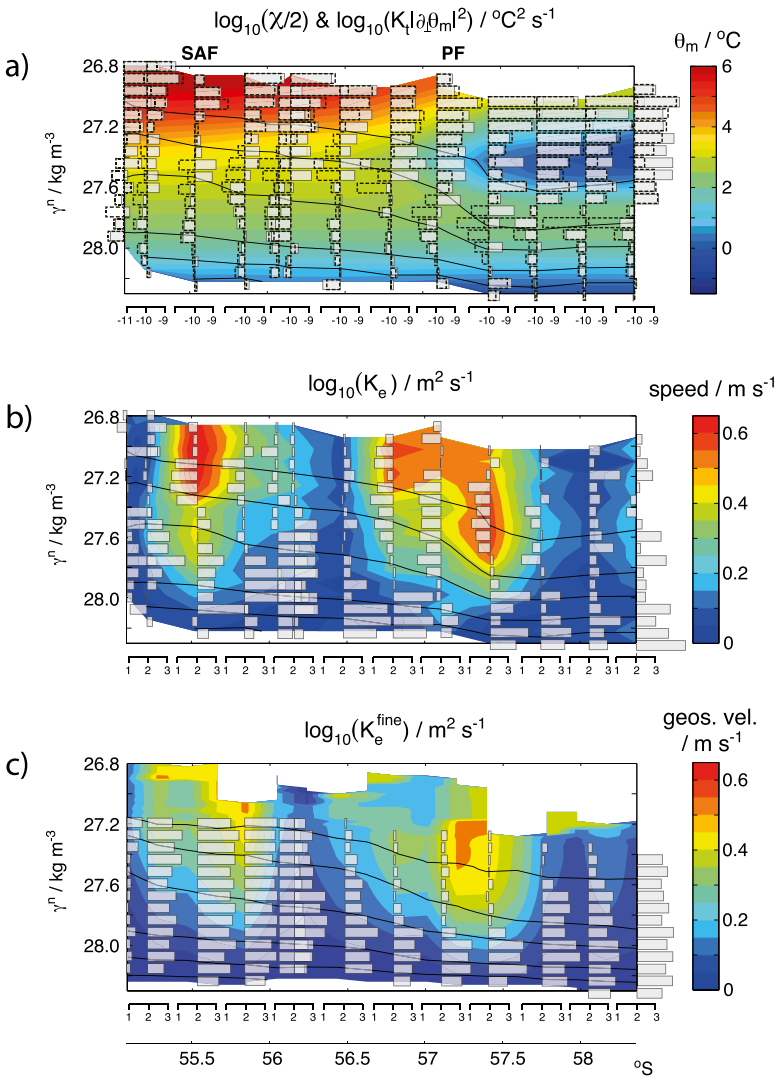

FIG. 6. Meridional sections along the JC69 occupation of the SR1b transect of (a) the rate of dissipation of temperature variance $\chi/2$ (gray bars) and the rate of dianeutral production of temperature variance $K_t|\partial_\perp\theta_m|^2$ (dashed bars), with θ_m shown by the background shading, and (b) K_e (gray bars), with LADCP-measured speed shown by the background shading. (c) A meridional section of K_e^{fine} (gray bars) along the SR1b section, estimated as explained in section 3, against a background of geostrophic velocity relative to the seafloor averaged over all the section repeats considered in the finestructure-based calculation. Pressure contours are superimposed on all panels and labeled in Fig. 4a. Frontal positions are indicated in the upper axis.

The contribution of dianeutral stirring to meridional overturning is estimated as the ratio between the dianeutral divergence of $K_t\partial_\perp\theta_m$ to $\partial_\parallel\theta_m$, as per (14). A section-characteristic profile of $K_t\partial_\perp\theta_m$ is computed as the isoneutral average of that variable for all stations in the section, barring the two farthest to the south (Fig. 8a), and its dianeutral divergence (Fig. 8b) is computed as a five-point running gradient to prevent grid-scale variability from dominating the divergence estimate. The term $\partial_\perp(K_t\partial_\perp\theta_m)$ is positive for isoneutrals lighter than $\gamma^n = 27.5\,\text{kg}\,\text{m}^{-3}$ and increases monotonically toward the surface mixed layer. At greater densities, $\partial_\perp(K_t\partial_\perp\theta_m)$ is negative and settles at a nearly constant value of $\sim 5\times10^{-10}\,^\circ\text{C}\,\text{s}^{-1}$. The implied profile of $\overline{v}^\dagger_\parallel$ (Fig. 8b) indicates significant northward flow at a rate of 0.3–1.3 mm s^{-1} in the $\gamma^n = 27.2\,\text{kg}\,\text{m}^{-3}$ density range and southward velocities of 0.3–0.6 mm s^{-1} in the $\gamma^n > 27.8\,\text{kg}\,\text{m}^{-3}$ class.

To conclude, we consider the component of meridional–isoneutral flow balanced by dianeutral advection of mean

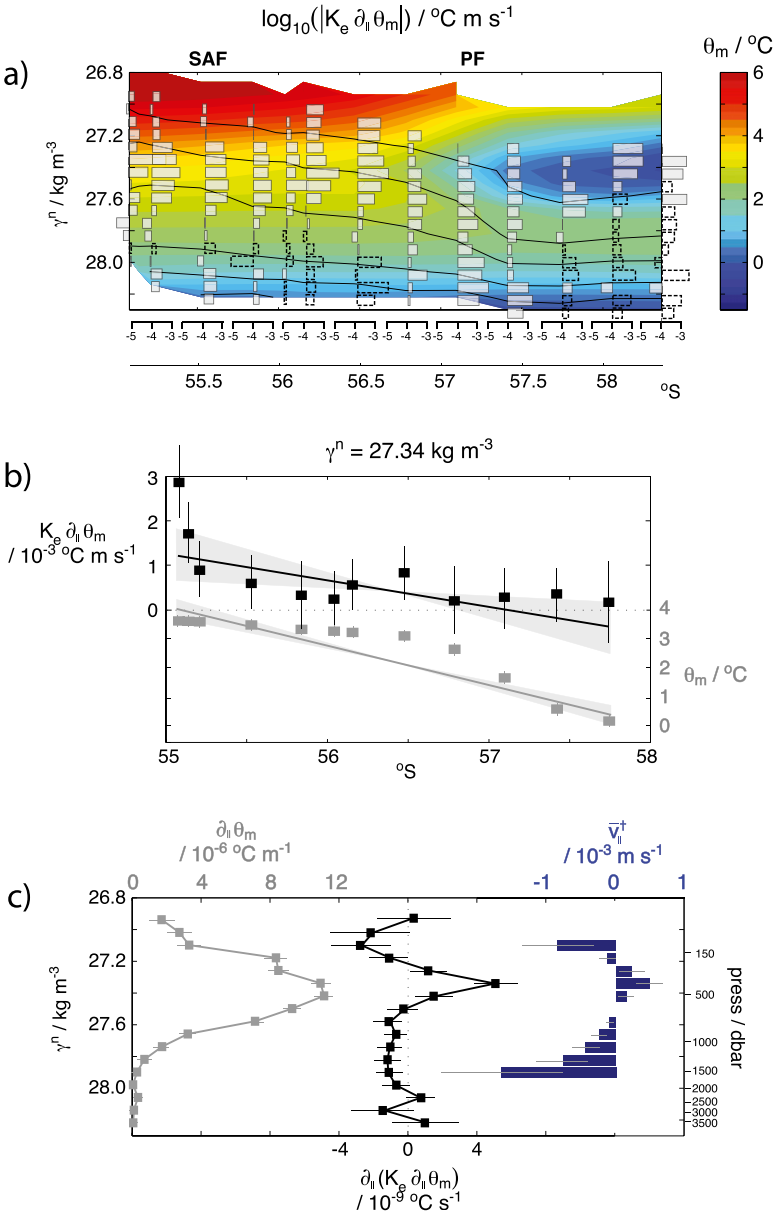

FIG. 7. (a) Meridional section along the JC69 occupation of the SR1b transect of $K_e\partial_\parallel\theta_m$. Positive (negative) values are indicated by gray (dashed) bars; θ_m is shown by the background shading. Pressure contours are superimposed in black and labeled in Fig. 4a. Frontal positions are indicated in the upper axis. (b) Illustrative meridional distributions of θ_m (gray squares) and $K_e\partial_\parallel\theta_m$ (black squares) for the $\gamma^n = 27.34\,\mathrm{kg\,m^{-3}}$ isoneutral in the JC69 data. The lines (with shaded uncertainties) show the linear fits to the measured distributions, which are used to estimate section-characteristic gradients of both variables (see section 5). (c) Section-characteristic profiles of $\partial_\parallel\theta_m$, $\partial_\parallel(K_e\partial_\parallel\theta_m)$, and the contribution to $\overline{v}^\dagger$ balanced by isoneutral stirring [only velocities corresponding to statistically significant values of $\partial_\parallel(K_e\partial_\parallel\theta_m)$ are shown]. The section-mean pressure profile of isoneutral surfaces is indicated on the right-hand axis.

potential temperature, that is, the third term on the right-hand side of (14). To quantify this component for the JC69 dataset, we first estimate the dianeutral residual-mean velocity $\overline{w}^\dagger_\perp$, averaged over the section. We apply expression (15) to the measured section-mean profiles of N^2 and ϵ (Fig. 9), where the vertical gradient of ϵ is calculated as a four-point running gradient to minimize the impact of grid-scale variability. The resulting $\overline{w}^\dagger_\perp$ is

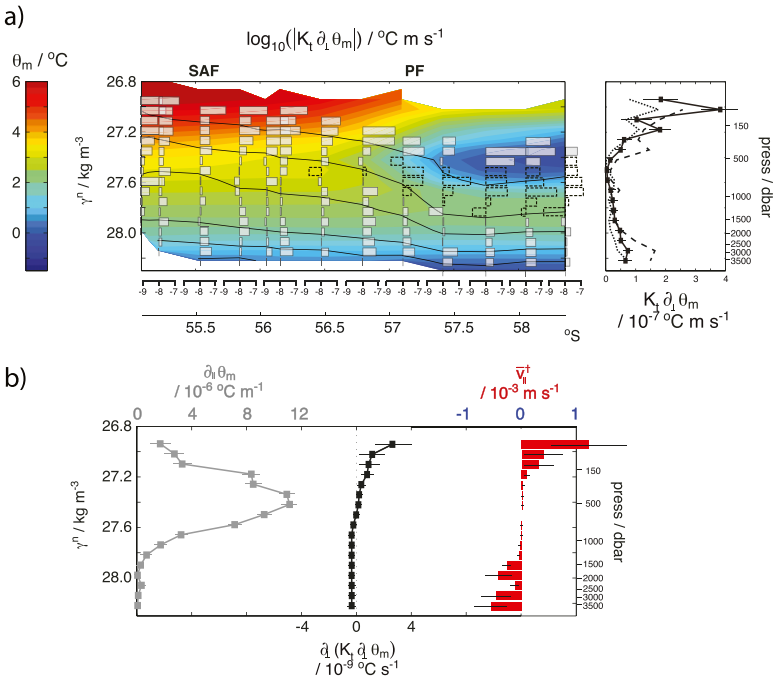

FIG. 8. (a) Meridional section along the JC69 occupation of the SR1b transect of $K_t\partial_\perp\theta_m$ (main panel). Positive (negative) values are indicated by gray (dashed) bars; θ_m is shown by the background shading. Pressure contours are superimposed in black and labeled in Fig. 4a. Frontal positions are indicated in the upper axis. The section-mean profile of $K_t\partial_\perp\theta_m$ is shown by the solid black line in the right-hand panel, with section-mean pressure values marked on that panel's right-hand axis. The dashed and dotted black lines display section-mean profiles of $K_t\partial_\perp\theta_m$ for the JR276 and JR281 transects, respectively. (b) Section-characteristic profiles of $\partial_\parallel\theta_m$, $\partial_\perp(K_t\partial_\perp\theta_m)$, and the contribution to $\overline{v}^\dagger$ balanced by dianeutral stirring [only velocities corresponding to statistically significant values of $\partial_\perp(K_t\partial_\perp\theta_m)$ are shown]. The section-mean pressure profile of isoneutral surfaces is indicated on the right-hand axis.

generally positive (indicating dianeutral upwelling), a consequence of the weakening of turbulent dissipation with depth over the upper half of Drake Passage. Whereas substantial dianeutral flow [$\overline{w}^\dagger_\perp \sim O(10^{-7})\,\mathrm{m\,s^{-1}}$] occurs in the lightest layers, elsewhere dianeutral velocity is modest, typically half an order of magnitude smaller than in the upper ocean. Projecting $\overline{w}^\dagger_\perp$ onto the mean isothermal slope in density space $\partial_\perp\theta_m/\partial_\parallel\theta_m$ yields an estimate of its importance relative to $\overline{v}^\dagger_\parallel$ (Fig. 9). This component typically exhibits southward flow and is small [$O(0.1)\,\mathrm{mm\,s^{-1}}$] relative to the contributions balanced by isoneutral and dianeutral stirring. An exception occurs in the lightest layers, where the contribution of dianeutral advection approaches values of $O(1)\,\mathrm{mm\,s^{-1}}$ and is comparable to the other terms.

The contributions of isoneutral stirring, dianeutral stirring, and dianeutral advection to the estimate of meridional–isoneutral flow are synthesized by Fig. 10. Contributions to $\overline{v}^\dagger_\parallel$ are plotted solely when they are distinct from zero within uncertainties, and the net rate of meridional–isoneutral flow is calculated by summing significant contributions only. The resulting overturning circulation is centered around $\gamma^n \approx 27.5\,\mathrm{kg\,m^{-3}}$ and implicates northward (southward) flows of 0.1–1 $\mathrm{mm\,s^{-1}}$ above (below) that density surface. Isoneutral and dianeutral stirring are found to play complementary roles in balancing meridional overturning across the large-scale thermohaline structure of the ACC, with isoneutral processes prevailing in the $27.2 < \gamma^n < 27.9\,\mathrm{kg\,m^{-3}}$ class and dianeutral processes dominating in the densest ($\gamma^n > 27.9\,\mathrm{kg\,m^{-3}}$) and lightest ($\gamma^n < 27.2\,\mathrm{kg\,m^{-3}}$) layers of the section. Dianeutral advection is a minor player in balancing meridional–isoneutral flow, except in the lightest layers ($\gamma^n < 27.2\,\mathrm{kg\,m^{-3}}$), where the estimated isoneutral circulation is of marginal significance.

6. Discussion

The picture of the rate, density structure, and mechanistic attribution of the overturning circulation across the ACC in Drake Passage emerging from the JC69 data and synthesized by Fig. 10 is grounded on two key

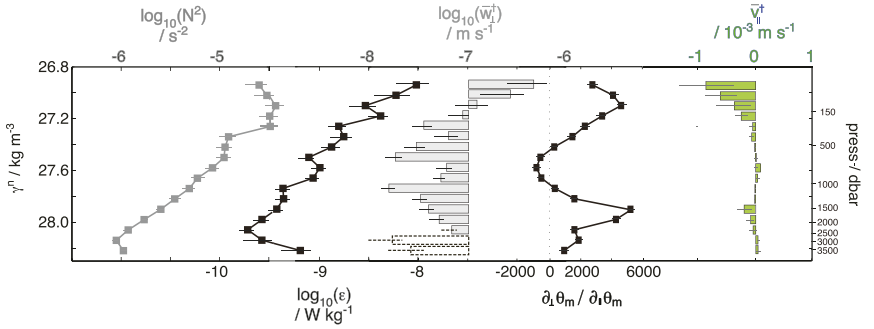

FIG. 9. Section-characteristic profiles of $\log_{10}(N^2)$, $\log_{10}(\varepsilon)$, $\log_{10}(\overline{w}^{\dagger}_{\perp})$, $\partial_{\perp}\theta_m/\partial_{\parallel}\theta_m$, and the contribution to $\overline{v}^{\dagger}$ balanced by dianeutral advection of mean potential temperature. Negative values of $\overline{w}^{\dagger}_{\perp}$ are indicated by dashed bars. The section-mean pressure profile of isoneutral surfaces is indicated on the right-hand axis.

features: a one to two orders of magnitude suppression of eddy-induced isoneutral stirring in the upper kilometer of the ACC frontal jets and a characteristic order of magnitude intensification of turbulent dissipation and dianeutral stirring in the subpycnocline and deepest layers of the ACC. The microstructure data for the JR276 and JR281 transects do not lend themselves to direct estimation of the meridional–isoneutral flow. Unfavorable weather conditions during those cruises resulted in considerable sampling gaps in one or both of the major ACC frontal jets, thereby preventing the robust estimation of the isoneutral gradients in (14). However, we will show in the following that the two key features underpinning the view of meridional overturning constructed from the JC69 measurements are quantitatively endorsed by the other two datasets.

An overview of the evidence of suppression of eddy-induced isoneutral stirring in the ACC frontal jets in all three microstructure transects is provided by Fig. 11. There, it is shown that in all transects the rate of dissipation of temperature variance χ increases modestly (typically by less than one order of magnitude) between areas of weak flow and the ACC frontal jet cores, where flow speeds of $\sim 0.5\,\mathrm{m\,s^{-1}}$ are regularly observed (Fig. 11a). The amplitude of the isoneutral gradient of θ_m exhibits a more marked, one order of magnitude enhancement between interfrontal and frontal zones. Since the rate of production of temperature variance by isoneutral stirring $K_e|\partial_{\parallel}\theta_m|^2$ scales with the square of the isoneutral gradient of θ_m, this observation implies that a systematic reduction of K_e at the ACC frontal jets of at least one order of magnitude must occur to close the temperature variance budget. This is corroborated by our analysis of all three microstructure transects, where a one to two orders of magnitude decrease in K_e is documented between areas of weak and strong flow (Fig. 11b).

It is the comparatively pronounced frontal reduction of K_e (relative to the more moderate frontal enhancement of $|\partial_{\parallel}\theta_m|$) that yields a northward increase in the isoneutral turbulent potential temperature flux in the WW/AAIW density class ($27.2 < \gamma^n < 27.5\,\mathrm{kg\,m^{-3}}$) and thereby balances the subduction of those waters at the PF and their subsequent northward flow [see (14)]. In contrast, southward flow in the Upper Circumpolar Deep Water (UCDW) class ($27.5 < \gamma^n < 27.9\,\mathrm{kg\,m^{-3}}$) is contingent on the degree of sensitivity of K_e to changes in speed for weak $[O(1)\,\mathrm{cm\,s^{-1}}]$ flows, which, when combined with the northward reduction to near-zero values in $|\partial_{\parallel}\theta_m|$, results in a southward enhancement in the isoneutral turbulent potential temperature flux within the UCDW layer. Thus, the functional dependence of K_e on flow speed is important in setting the

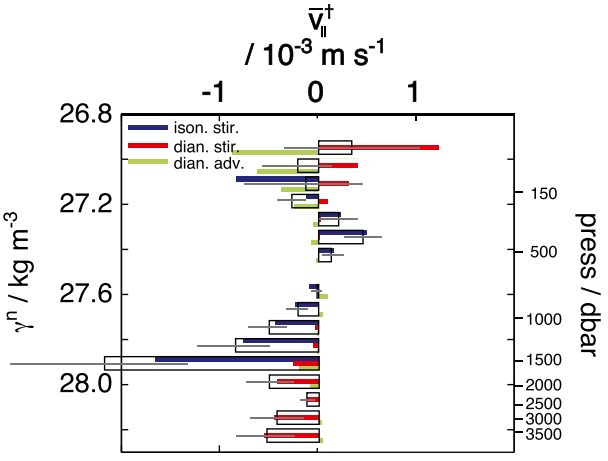

FIG. 10. Section-characteristic profile for the JC69 occupation of the SR1b transect of $\overline{v}^{\dagger}_{\parallel}$ (open bars, with error bars), with contributions balanced by isoneutral stirring, dianeutral stirring, and dianeutral advection respectively indicated by blue, red, and green bars. The section-mean pressure profile of isoneutral surfaces is indicated on the right-hand axis.

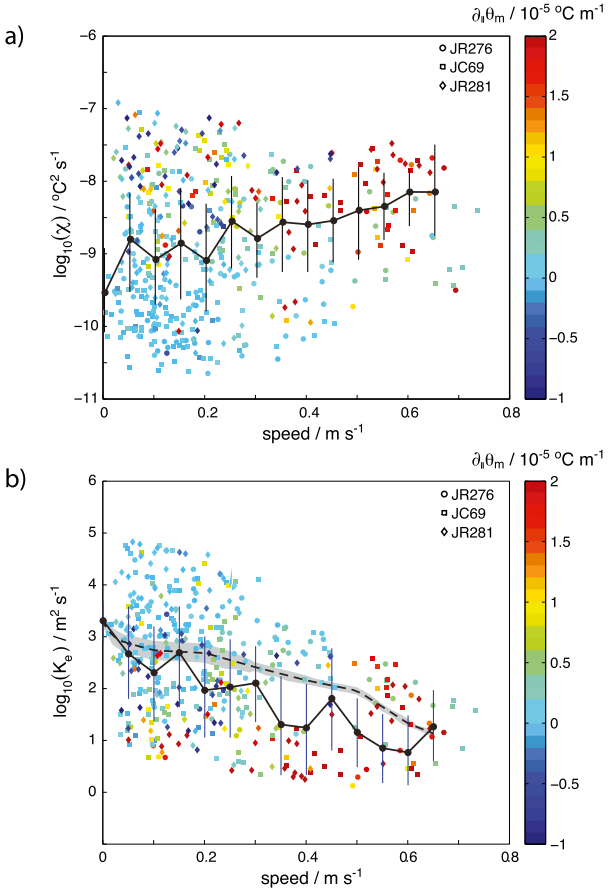

FIG. 11. Estimates of (a) χ and (b) K_e (colored symbols, shaded by $\partial_\parallel\theta_m$) displayed as a function of LADCP-measured speed for the three SR1b section occupations with microstructure data (indicated by different symbol shapes). Averages of $\log_{10}(\chi)$ and $\log_{10}(K_e)$ in speed bins of 0.05 m s^{-1} width are shown by the black circles and thick line, with the thin vertical lines denoting the standard deviation of individual $\log_{10}(\chi)$ and $\log_{10}(K_e)$ estimates within each speed bin. The dashed line in (b) shows the decay of K_e with increasing speed predicted by the inverse stirring suppression factor of FN10, using the mean microstructure-based K_e value at zero speed and the average altimetry-derived (depth dependent) eddy kinetic energy in each speed bin [updated from NG11]. The gray shading indicates the range of predicted K_e values associated with one standard deviation of the individual estimates of eddy kinetic energy in each speed bin.

observed meridional overturning across the ACC's mean thermohaline structure. A significantly less (more) acute sensitivity of K_e to flow speed at relatively high (low) flow speeds would be associated with a distinct pattern of Southern Ocean overturning, thermohaline configuration, or both.

The functional dependence of K_e on the properties of the mean flow and the mesoscale eddy field was recently investigated by FN10 on the basis of a baroclinic quasi-geostrophic model of weakly nonlinear eddy perturbations embedded in a broad zonal jet (see also theoretical discussion in NG11). They derived the approximate scaling

$$K_e \approx \frac{K_e^{\text{Taylor}}}{1 + 4U_m^2 \text{EKE}^{-1}}, \tag{16}$$

where $K_e^{\text{Taylor}} \propto \text{EKE}\gamma^{-1}$ is Taylor's (1921) classical definition of the eddy diffusivity for a quasi-homogeneous, isotropic, turbulent eddy field with no mean flow; γ^{-1} is an eddy decorrelation (damping) time scale; and U_m is the speed of the zonal mean flow. Equation (16) makes two elementary predictions: that K_e is enhanced by energetic eddy fields and that it is suppressed by intense mean flows. Our microstructure-based estimates of K_e exhibit a broad quantitative consistence with these predictions (Fig. 11b) and thereby suggest that the simple representation of the eddy stirring process in the work of FN10 captures the essential properties of the eddy-induced cascade of thermohaline variance in the area of our observations. We note, however, that this comparison has limited testing value, as there is a close association in our data between large (small) microstructure-based estimates of K_e and weak (strong) isoneutral gradients of θ_m, which are linked to high (low) mean flow speeds through thermal wind. While this association would be expected if eddy stirring eroded isoneutral property gradients in areas of low mean flow, as predicted by the FN10 scaling, a conclusive validation of the scaling would require more extensive sampling of regimes with small (large) K_e and weak (strong) isoneutral gradients of θ_m.

The general consistence between our K_e diagnostics and the theoretical scaling of FN10 echoes recent successful tests of their model at the mesoscale (i.e. the scale of turbulent production of tracer variance; see FN10 and Klocker and Abernathey 2014). Similar to those assessments, which were based on the advection of a synthetic tracer by satellite altimetry-derived velocity fields, the analysis of thermohaline finestructure measurements of NG11 provided broad endorsement of the scaling. Note, though, that the results of NG11 also pointed to a significant shortcoming in the theory's predictions, which appears at odds with the findings of the present work. To illustrate this issue, we consider the distribution of the finestructure-derived estimate of K_e for the SR1b section (updated from NG11; see section 3b), superimposed on the seafloor-referenced geostrophic velocity averaged over all the section repeats considered in the finestructure-based calculation (Fig. 6c). The mean geostrophic velocity structure of the SAF and PF jets resembles that in the LADCP survey conducted during the JC69 cruise (Fig. 4e), although peak speeds at the jet cores are typically higher

by $\sim 0.1\,\mathrm{m\,s^{-1}}$ in the LADCP data. A comparison with the distribution of the microstructure-derived K_e (Fig. 6b) reveals that the two sets of K_e estimates have two main features in common, namely, the occurrence of higher-quartile diffusivities of $O(10^3)\,\mathrm{m^2\,s^{-1}}$, which are in line with estimates based on the dispersion of a natural tracer in the vicinity of the SR1b transect (Naveira Garabato et al. 2007), and the pronounced reduction of K_e at the core of the PF jet relative to its surroundings. However, they also exhibit two clear differences, specifically, the occurrence of lower-quartile diffusivities that are one order of magnitude larger in the finestructure case [$O(10^2)\,\mathrm{m^2\,s^{-1}}$, cf. $O(10)\,\mathrm{m^2\,s^{-1}}$ for microstructure-derived diffusivities] and the absence of a reduction of K_e at the core of the SAF jet in the finestructure case.

While the former difference is likely to arise from the higher noise floor of the finestructure calculation [which is affected by the generation of thermohaline finestructure by processes other than isoneutral eddy stirring (Ferrari and Polzin 2005; NG11)], the latter difference provides insight into how the downscale cascade of thermohaline variance in the ACC deviates from the assumptions adopted in estimating K_e through the two approaches examined here. These approaches focus on opposite ends of the cascade [the finestructure method on the lateral scales of thermohaline variance production, which are larger than the first baroclinic Rossby radius (Holloway and Kristmannsson 1984; Held and Larichev 1996; Smith et al. 2002); the microstructure method on the scales of dissipation, of $O(1)$ cm], yet both assume that a local balance between production and dissipation exists. This assumption is formally invalidated by our results, which indicate that the time scale of temperature variance dissipation in Drake Passage,

$$\tau \sim \theta^2_{\mathrm{rms}}/\chi, \tag{17}$$

is typically of $O(1)$ yr (Fig. 5a, right). Given a characteristic ACC speed of $O(0.1)\,\mathrm{m\,s^{-1}}$ (Fig. 3c), an advection of variance by $O(1000)$ km along the ACC between its being produced and dissipated is implied, inconsistent with the local balance assumption. It is thus likely that the absence of a reduction of K_e^{fine} at the core of the SAF jet stems from the invalidity of this assumption, as the northern edge of the SR1b section lies $O(100)$ km downstream of an area of intense mesoscale eddy growth and recirculation in the Yaghan basin (Fig. 2; Klocker and Abernathey 2014). More fundamentally, the long persistence of thermohaline variance in the ACC suggests that our microstructure-derived K_e along the SR1b transect should not be interpreted as a strictly local diagnostic but as an along-stream spatiotemporal average over scales of O[(1000) km; (1) yr] west of the section.

The longevity of thermohaline variance in the ACC provides insight into why the potential temperature variance budget in (6), which entails approximations that are difficult to justify a priori (section 2a), yields a realistic distribution of K_e when applied to local hydrographic and microstructure observations. The relatively inefficient downscale cascade of thermohaline variance implied by the variance's long persistence suggests that the prominent along-stream variations known to occur in variance production (e.g., Thompson and Naveira Garabato 2014) are slow to be imprinted on the large-scale mean θ–S relationship of the ACC and are unlikely to result in analogous marked changes in variance dissipation. Thus, the large-scale mean θ_m field entering (6), derived from measurements at a specific section, is representative of a sector extending $O(1000)$ km upstream and not just of local value. We suggest that this property underpins the success of the gravest empirical mode approaches in representing the zonal evolution of the ACC's hydrographic structure from scattered observations (Meijers et al. 2011). Similarly, local measurements of χ at our transect arguably reflect variance production over a substantial upstream region, greater than the $O(100$–$500)$ km horizontal scale below which the assumptions made in deriving (6) may break down (section 2a). We conclude that the long persistence of thermohaline variance in the ACC makes it possible to obtain meaningful information on the patterns of cross-stream isoneutral stirring from localized measurements.

As remarked above, the significant contribution of dianeutral stirring to meridional overturning across the lightest and densest layers of the ACC documented in the JC69 dataset is contingent on a characteristic order of magnitude enhancement of the rates of turbulent dissipation and dianeutral stirring in those layers. Analysis of the JR276 and JR281 microstructure measurements corroborates the persistent nature of this feature, as illustrated by the comparison of section-mean profiles of the dianeutral turbulent potential temperature flux $K_t\partial_\perp\theta_m$, conducted in Fig. 8a (right-hand panel). All three realizations of $K_t\partial_\perp\theta_m$ exhibit a minimum of $O(10^{-8})\,^\circ\mathrm{C\,m\,s^{-1}}$ near the $\gamma^n = 27.5\,\mathrm{kg\,m^{-3}}$ isoneutral, within the 500–1000-m depth range, and increase to values of $O(10^{-7})\,^\circ\mathrm{C\,m\,s^{-1}}$ around the permanent pycnocline and below 2000 m. Whereas the upward intensification of $K_t\partial_\perp\theta_m$ is indistinguishable (within uncertainties) in the three profiles, its downward enhancement is significantly more pronounced (by approximately a factor of 2) in the JR276 data.

The distinctive vertical distribution of $K_t\partial_\perp\theta_m$ may arguably be related to the existence of two primary energy sources for the internal wave field in Drake Passage: the wind-induced generation of near-inertial waves in the surface mixed layer and the radiation of internal lee waves as the ACC eddy field impinges on rough seafloor topography. The breaking of downward-propagating near-inertial waves generated by wind forcing of the upper ocean has been shown to sustain elevated levels of turbulent dissipation at subpycnocline depths of typically less than ~1000 m, both in Drake Passage (Sheen et al. 2013; Kilbourne and Girton 2015) and elsewhere in the ACC (Waterman et al. 2013; Forryan et al. 2015). Conversely, the upward radiation and breaking of eddy-generated internal lee waves has been found to underpin the intensification of turbulent dissipation within 1–2 km of the seafloor in ACC regions of complex bathymetry, including Drake Passage (Naveira Garabato et al. 2004; Nikurashin and Ferrari 2010; St. Laurent et al. 2012; Sheen et al. 2013; Brearley et al. 2013). The significant enhancement of $K_t\partial_\perp\theta_m$ at depth during JR276 may in fact be explained by an eddy-induced energization of the internal wave field over a 7-month period encompassing the time of that cruise (Sheen et al. 2014).

7. Conclusions

We have shown that a picture of mixing and overturning across a region of the ACC can be constructed from a relatively modest number of (shear and temperature) microstructure profiles. The microstructure measurements are analyzed in the framework of a triple decomposition applied to the temperature variance budget [(6)], in which the dissipation of variance by molecular mixing is balanced by the production of variance associated with mesoscale eddy-induced isoneutral stirring and with dianeutral stirring by small-scale turbulence, acting on the large-scale mean state. This balance is established on a time scale of $O(1)$ yr, such that newly produced variance is advected downstream by the ACC over $O(1000)$ km before being dissipated. Our overarching result is that the rates of isoneutral and dianeutral stirring exhibit distinct, characteristic, relatively abrupt variations that are pivotal to the sustainment of an overturning circulation of $O(1)$ mm s^{-1} across the ACC's mean thermohaline structure. The overturning is found to consist of northward flow above the $\gamma^n \approx 27.5$ kg m^{-3} isoneutral and southward flow below. Isoneutral and dianeutral stirring play complementary roles in balancing the overturning, with isoneutral processes prevailing in the $27.2 < \gamma^n < 27.9$ kg m^{-3} class (encompassing WW/AAIW and UCDW) and dianeutral processes dominating in the lightest ($\gamma^n < 27.2$ kg m^{-3}, which mainly includes waters below the base of the seasonal pycnocline) and densest [$\gamma^n > 27.9$ kg m^{-3}, largely composed of Lower Circumpolar Deep Water (LCDW)] layers.

The single most prominent feature of the distribution of eddy stirring across the ACC is its suppression by the strong mean flow within the upper ~1 km of ACC frontal jets, a phenomenon that may be understood using simple kinematic arguments (FN10; NG11). Thermohaline variance is observed to be injected into the approximate 500–1000-m depth range of the ACC interior from frontal sites where isoneutrals outcrop into the remnant winter mixed layer, found at depths of 100–200 m in our study region. Subduction and equatorward flow of these waters is facilitated by the marked suppression of eddy stirring at the fronts, which overcomes the equatorward reduction in the isoneutral temperature gradient to yield an equatorward enhancement of the isoneutral turbulent potential temperature flux. We suggest that frontal suppression of eddy stirring may, in this way, underpin the general observation that density classes outcropping at fronts in winter are selected for subduction into the interior across the global ocean (Speer and Forget 2013).

The prevalent role of dianeutral stirring by small-scale turbulence in balancing meridional flow in the lightest and densest layers of the ACC interior relates to the proximity of those layers to the two primary sources of internal waves in the study region, which results in a pronounced intensification of small-scale turbulence in the uppermost ~1 km and deepest 1–2 km. While this stress on the significance of dianeutral stirring in the Southern Ocean overturning appears at odds with the extensive characterization of the interior circulation in terms of adiabatic processes, our findings resonate with those of several recent studies. For example, Sloyan et al. (2010) show that small-scale turbulence below the seasonal pycnocline exerts a major preconditioning influence on wintertime SAMW formation in the southeast Pacific, in line with our conclusion that water mass transformations at that level are controlled by near-inertial wave breaking and possibly other dianeutral processes in the transition layer. Similarly, the likely importance of dianeutral mixing in the deep Southern Ocean in sustaining abyssal overturning is highlighted by several authors (Ito and Marshall 2008; Nikurashin and Ferrari 2013; Broadbridge et al. 2015, manuscript submitted to *Geophys. Res. Lett.*).

Our estimate of the regional overturning flow is comparable in structure and magnitude to that implicit in the zonally integrated Southern Ocean overturning

diagnosed in many realistic eddy-permitting numerical models [see Marshall and Speer (2012) and Rintoul and Naveira Garabato (2013) and references therein] and from a circumpolar hydrographic climatology (Zika et al. 2009). The latter study is grounded in a formulation analogous to (14) and shows that a plausible zonally integrated overturning across the ACC's mean thermohaline structure can be sustained in the absence of isoneutral gradients in the rate of eddy stirring. This apparent contradiction with our findings may be resolved by considering the very different spatiotemporal averaging in Zika et al.'s circumpolar-integrated application, which, unlike our approach, smears out ACC frontal features and their eddy stirring suppression signatures.

Acknowledgments. The DIMES experiment was funded by the U.K. Natural Environment Research Council (NERC) and the U.S. National Science Foundation (NSF). ACNG acknowledges the support of a Philip Leverhulme Prize, the Royal Society, and the Wolfson Foundation. JDZ acknowledges the support of a NERC Research Fellowship.

APPENDIX

Uncertainty in the Microstructure-Based Diagnostics of the Rates of Mixing and Overturning

The uncertainties in our microstructure-based diagnostics of K_t, K_e, and $\overline{v}^{\dagger}_{\parallel}$ are quantified in two stages: The first involves the estimation of uncertainties in the microstructure variables (ϵ and χ) and in K_t and $\overline{w}^{\dagger}_{\perp}$, which are straightforwardly derived from ϵ. The second entails the assessment of how the combination of these uncertainties with those associated with the definition of θ_m affects our estimates of K_e and $\overline{v}^{\dagger}_{\parallel}$. These two stages are described sequentially in this appendix.

a. Uncertainty in ϵ, χ, K_t, and $\overline{w}^{\dagger}_{\perp}$

The uncertainties of bin-averaged ϵ and χ values are estimated here as 90% confidence intervals via a bootstrap method (Efron and Gong 1983), following Waterman et al. (2013). The quoted confidence intervals represent the fifth largest and smallest values of 100 sums formed by randomly sampling the data. Uncertainties in ϵ and χ computed in this manner characteristically decrease from a factor of 2–3 in the lightest, thinnest layers to less than a factor of 2 for layers deeper than ~500 m. While these uncertainties are not displayed in section plots for reasons of clarity, they are quoted as and when appropriate and are propagated through to derived variables.

The uncertainty in bin-averaged K_t, which is proportional to the ratio of ϵ to N^2 [see (7)], is dominated by the uncertainty in ϵ and is only slightly augmented (typically by less than a factor of 2) by uncertainty in the computation of bin-averaged N^2. The fractional uncertainty in section-averaged $\overline{w}^{\dagger}_{\perp}$ is very close to that in K_t, as the additional error introduced by vertical differentiation of ϵ is largely offset by averaging along the section.

b. Uncertainty in θ_m, K_e, and $\overline{v}^{\dagger}_{\parallel}$

The uncertainty in θ_m is estimated at any one bin in each section occupation as the rms value of the differences between the original potential temperature measurements within that bin and the local θ_m computed from all the stations in the transect save the station of the bin under consideration. The resulting error fields reveal negligible (typically <5% of the range of temperatures found along the relevant isoneutral) uncertainties in θ_m at depths in excess of ~300 m, with more substantial uncertainties (of up to 30% of the temperature range of the isoneutral) at the locations of isoneutral outcrops into the remnant winter mixed layer. Isoneutral and dianeutral gradients of θ_m are similarly most uncertain near these outcrop sites, with their magnitudes (not their signs) exhibiting some sensitivity to the degree of smoothing of the cubic spline used in defining θ_m. Note, though, that the highest uncertainties in the gradient magnitudes never exceed a factor of 2 and so can be regarded as modest relative to uncertainties in microstructure-based variables.

The uncertainty in K_e [see (8)] is primarily dictated by those in χ and K_t, with errors in the gradients of θ_m contributing the most at the ~20% level at outcrop sites. Assuming uncertainties in χ and K_t to be independent, their combined effect yields characteristic uncertainties in K_e of a factor of 3–4 around and above the base of the winter mixed layer (i.e., in the uppermost ~300 m) and of a factor of 2–3 at greater depth. The validity of these uncertainty estimates is endorsed by computations of the ratio $2K_t|\partial_{\perp}\theta_m|^2/\chi$ in interior layers with near-zero isoneutral gradients in θ_m ($|\partial_{\parallel}\theta_m| < 2 \times 10^{-6}\,^{\circ}\mathrm{C\,m^{-1}}$), for which the isoneutral production of temperature variance is expected to be small. Approximately 91% of bins exhibit values of this ratio in the range $\frac{1}{3}$–3, thereby suggesting that errors in our calculation of K_e do not generally exceed the levels quoted above.

The uncertainty in our estimates of the contribution of isoneutral stirring to $\overline{v}^{\dagger}_{\parallel}$ is dominated by the uncertainty in K_e. This is because K_e largely dictates the sign and magnitude of $\partial_{\parallel}(K_e\partial_{\parallel}\theta_m)$ (see section 6) and has a substantially greater fractional uncertainty than $\partial_{\parallel}\theta_m$. To optimize the robustness of $\partial_{\parallel}(K_e\partial_{\parallel}\theta_m)$ estimates, we do

not attempt to calculate isoneutral gradients between stations but instead conduct a least squares linear fit to the distribution of $K_e\partial_{\|}\theta_m$ along the section in each density class. This ensures that only the large-scale structure in $K_e\partial_{\|}\theta_m$, resolved by many stations, is taken into account in the computation of $\overline{v}^{\dagger}_{\|}$ and that the detrimental impact of errors in K_e is minimized. Values of the contribution of isoneutral stirring to $\overline{v}^{\dagger}_{\|}$ are only considered for isoneutral layers for which the slope of the fitted line is statistically different from zero.

The uncertainties in our estimates of the contributions of dianeutral stirring and dianeutral advection to $\overline{v}^{\dagger}_{\|}$ are modest in comparison with the errors associated with the isoneutral stirring term. They are chiefly dependent on the uncertainty in the dianeutral gradient of K_t (for the dianeutral stirring term) or in the dianeutral gradient of ϵ (for the dianeutral advection term), with errors in $\partial_{\perp}\theta_m$ accounting for at most a ~10% change in the magnitude of the dianeutral contributions to $\overline{v}^{\dagger}_{\|}$ in the lightest layers. For the dianeutral stirring term, statistical robustness is maximized by permitting only the large-scale structure of $\partial_{\perp}(K_t\partial_{\perp}\theta_m)$ to enter the calculation of the dianeutral contribution to $\overline{v}^{\dagger}_{\|}$ [(14)]. This is achieved by computing isoneutral averages of $K_t\partial_{\perp}\theta_m$ along the section prior to dianeutral differentiation and by calculating the dianeutral divergence of that section-averaged profile as a five-point running gradient. This exercise yields consistently significant estimates of $\partial_{\perp}(K_t\partial_{\perp}\theta_m)$, as illustrated by the favorable comparison between $K_t\partial_{\perp}\theta_m$ profiles estimated from different datasets (Fig. 7a).

REFERENCES

Abernathey, R. P., and J. Marshall, 2013: Global surface eddy diffusivities derived from satellite altimetry. *J. Geophys. Res. Oceans*, **118**, 901–916, doi:10.1002/jgrc.20066.

——, ——, M. Mazloff, and E. Shuckburgh, 2010: Enhancement of mesoscale eddy stirring at steering levels in the Southern Ocean. *J. Phys. Oceanogr.*, **40**, 170–184, doi:10.1175/2009JPO4201.1.

Armi, L., and H. Stommel, 1983: Four views of a portion of the North Atlantic subtropical gyre. *J. Phys. Oceanogr.*, **13**, 828–857, doi:10.1175/1520-0485(1983)013<0828:FVOAPO>2.0.CO;2.

Brearley, J. A., K. L. Sheen, A. C. Naveira Garabato, D. A. Smeed, and S. N. Waterman, 2013: Eddy-induced modulation of turbulent dissipation over rough topography in the Southern Ocean. *J. Phys. Oceanogr.*, **43**, 2288–2308, doi:10.1175/JPO-D-12-0222.1.

Davis, R. E., 1994: Diapycnal mixing in the ocean: The Osborn–Cox model. *J. Phys. Oceanogr.*, **24**, 2560–2576, doi:10.1175/1520-0485(1994)024<2560:DMITOT>2.0.CO;2.

Efron, B., and G. Gong, 1983: A leisurely look at the bootstrap, the jackknife, and cross-validation. *Amer. Stat.*, **37**, 36–48, doi:10.2307/2685844.

Ferrari, R., and K. L. Polzin, 2005: Finescale structure of the *T*–*S* relation in the eastern North Atlantic. *J. Phys. Oceanogr.*, **35**, 1437–1454, doi:10.1175/JPO2763.1.

——, and M. Nikurashin, 2010: Suppression of eddy mixing across jets in the Southern Ocean. *J. Phys. Oceanogr.*, **40**, 1501–1519, doi:10.1175/2010JPO4278.1.

——, J. C. McWilliams, V. M. Canuto, and M. Dubovikov, 2008: Parameterization of eddy fluxes near oceanic boundaries. *J. Climate*, **21**, 2770–2789, doi:10.1175/2007JCLI1510.1.

Forryan, A., A. C. Naveira Garabato, K. L. Polzin, and S. N. Waterman, 2015: Rapid injection of near-inertial shear into the stratified upper ocean at an Antarctic Circumpolar Current front. *Geophys. Res. Lett.*, **42**, 3431–3441, doi:10.1002/2015GL063494.

Garrett, C., 2001: Stirring and mixing: What are the rate-controlling processes? *Stirring to Mixing in a Stratified Ocean: Proc. 'Aha Huliko'a Winter Workshop*, Honolulu, HI, University of Hawai'i at Mānoa, 1–8.

Held, I., and V. D. Larichev, 1996: A scaling theory for horizontally homogeneous, baroclinically unstable flow on a beta-plane. *J. Atmos. Sci.*, **53**, 946–952, doi:10.1175/1520-0469(1996)053<0946:ASTFHH>2.0.CO;2.

Holloway, G., and S. S. Kristmannsson, 1984: Stirring and transport of tracer fields by geostrophic turbulence. *J. Fluid Mech.*, **141**, 27–50, doi:10.1017/S0022112084000720.

Ito, T., and J. C. Marshall, 2008: Control of lower limb circulation in the Southern Ocean by dianeutral mixing and mesoscale eddy transfer. *J. Phys. Oceanogr.*, **38**, 2832–2845, doi:10.1175/2008JPO3878.1.

Jackett, D. R., and T. J. McDougall, 1997: A neutral density variable for the world's oceans. *J. Phys. Oceanogr.*, **27**, 237–263, doi:10.1175/1520-0485(1997)027<0237:ANDVFT>2.0.CO;2.

Joyce, T. M., 1977: A note on the lateral mixing of water masses. *J. Phys. Oceanogr.*, **7**, 626–629, doi:10.1175/1520-0485(1977)007<0626:ANOTLM>2.0.CO;2.

Kilbourne, B. F., and J. B. Girton, 2015: Quantifying high-frequency wind energy flux into near-inertial motions in the southeast Pacific. *J. Phys. Oceanogr.*, **45**, 369–386, doi:10.1175/JPO-D-14-0076.1.

Klocker, A., and T. J. McDougall, 2010: Influence of the nonlinear equation of state on global estimates of dianeutral advection and diffusion. *J. Phys. Oceanogr.*, **40**, 1690–1709, doi:10.1175/2010JPO4303.1.

——, and R. Abernathey, 2014: Estimating mesoscale eddy diffusion coefficients from satellite observations. *J. Phys. Oceanogr.*, **44**, 1030–1046, doi:10.1175/JPO-D-13-0159.1.

Lu, J., and K. Speer, 2010: Topography, jets, and eddy mixing in the Southern Ocean. *J. Mar. Res.*, **68**, 479–502, doi:10.1357/002224010794657227.

Marshall, J., and K. G. Speer, 2012: Closure of the meridional overturning circulation through Southern Ocean upwelling. *Nat. Geosci.*, **5**, 171–180, doi:10.1038/ngeo1391.

Maximenko, N., P. Niiler, L. Centurioni, M.-H. Rio, and O. Melnichenko, 2009: Mean dynamic topography of the ocean from satellite and drifting buoy data using three different techniques. *J. Atmos. Oceanic Technol.*, **26**, 1910–1919, doi:10.1175/2009JTECHO672.1.

Meijers, A. J. S., N. L. Bindoff, and S. R. Rintoul, 2011: Estimating the four-dimensional structure of the Southern Ocean using satellite altimetry. *J. Atmos. Oceanic Technol.*, **28**, 548–568, doi:10.1175/2010JTECHO790.1.

Naveira Garabato, A. C., 2009: Cruise report RRS James Cook JC029 (SOFine). National Oceanography Centre Southampton Cruise Rep. 35, 216 pp.

——, K. L. Polzin, B. A. King, K. J. Heywood, and M. Visbeck, 2004: Widespread intense turbulent mixing in the Southern Ocean. *Science*, **303**, 210–213, doi:10.1126/science.1090929.

——, D. P. Stevens, A. J. Watson, and W. Roether, 2007: Short-circuiting of the overturning circulation in the Antarctic Circumpolar Current. *Nature*, **447**, 194–197, doi:10.1038/nature05832.

——, R. Ferrari, and K. L. Polzin, 2011: Eddy stirring in the Southern Ocean. *J. Geophys. Res.*, **116**, C09019, doi:10.1029/2010JC006818.

Nikurashin, M., and R. Ferrari, 2010: Radiation and dissipation of internal waves generated by geostrophic motions impinging on small-scale topography: Application to the Southern Ocean. *J. Phys. Oceanogr.*, **40**, 2025–2042, doi:10.1175/2010JPO4315.1.

——, and ——, 2013: Overturning circulation driven by breaking internal waves in the deep ocean. *Geophys. Res. Lett.*, **40**, 3133–3137, doi:10.1002/grl.50542.

Oakey, N. S., 1982: Determination of the rate of dissipation of turbulent energy from simultaneous temperature and velocity shear microstructure measurements. *J. Phys. Oceanogr.*, **12**, 256–271, doi:10.1175/1520-0485(1982)012<0256:DOTROD>2.0.CO;2.

Osborn, T. R., 1980: Estimates of the local rate of vertical diffusion from dissipation measurements. *J. Phys. Oceanogr.*, **10**, 83–89, doi:10.1175/1520-0485(1980)010<0083:EOTLRO>2.0.CO;2.

——, and C. Cox, 1972: Oceanic fine structure. *Geophys. Fluid Dyn.*, **3**, 321–335, doi:10.1080/03091927208236085.

Plumb, R. A., and R. Ferrari, 2005: Transformed Eulerian-mean theory. Part I: Nonquasigeostrophic theory for eddies on a zonal-mean flow. *J. Phys. Oceanogr.*, **35**, 165–174, doi:10.1175/JPO-2669.1.

Polzin, K. L., and E. T. Montgomery, 1996: Deep microstructure profiling with the High Resolution Profiler. *Proc. Microstructure Sensors Workshop*, Mt. Hood, OR, Office of Naval Research, 109–115.

——, and R. Ferrari, 2004: Isopycnal dispersion in NATRE. *J. Phys. Oceanogr.*, **34**, 247–257, doi:10.1175/1520-0485(2004)034<0247:IDIN>2.0.CO;2.

Prandtl, L., 1925: Bericht über untersuchungen zur ausgebildeten turbulenz. *Z. Angew. Math. Mech.*, **5**, 136–139.

Rintoul, S. R., and A. C. Naveira Garabato, 2013: Dynamics of the Southern Ocean circulation. *Ocean Circulation and Climate: A 21st Century Perspective*, G. Siedler et al., Eds., Academic Press, 471–488.

Sallée, J.-B., 2013: Cruise report JR 281: RRS James Clark Ross, 14 March–26 April 2013. British Antarctic Survey, 150 pp. [Available online at https://www.bodc.ac.uk/data/information_and_inventories/cruise_inventory/report/jr281.pdf.]

——, K. Speer, and S. R. Rintoul, 2011: Mean flow and topographic control on surface eddy mixing in the Southern Ocean. *J. Mar. Res.*, **69**, 753–777, doi:10.1357/002224011799849408.

Sheen, K. L., and Coauthors, 2013: Rates and mechanisms of turbulent dissipation and mixing in the Southern Ocean: Results from the Diapycnal and Isopycnal Mixing Experiment in the Southern Ocean (DIMES). *J. Geophys. Res. Oceans*, **118**, 2774–2792, doi:10.1002/jgrc.20217.

——, and Coauthors, 2014: Changes in Southern Ocean abyssal mixing on climatic timescales. *Nat. Geosci.*, **7**, 577–582, doi:10.1038/ngeo2200.

Sloyan, B. M., L. D. Talley, T. K. Chereskin, R. Fine, and J. Holte, 2010: Antarctic Intermediate Water and Subantarctic Mode Water formation in the southeast Pacific: The role of turbulent mixing. *J. Phys. Oceanogr.*, **40**, 1558–1574, doi:10.1175/2010JPO4114.1.

Smith, K. S., and J. Marshall, 2009: Evidence for enhanced eddy mixing at middepth in the Southern Ocean. *J. Phys. Oceanogr.*, **39**, 50–69, doi:10.1175/2008JPO3880.1.

——, G. Boccaletti, C. C. Henning, I. Marinov, C. Y. Tam, I. M. Held, and G. K. Vallis, 2002: Turbulent diffusion in the geostrophic inverse cascade. *J. Fluid Mech.*, **469**, 13–48, doi:10.1017/S0022112002001763.

Speer, K. G., and G. Forget, 2013: Global distribution and formation of mode waters. *Ocean Circulation and Climate: A 21st Century Perspective*, G. Siedler et al., Eds., Academic Press, 211–226.

St. Laurent, L., A. C. Naveira Garabato, J. R. Ledwell, A. M. Thurnherr, J. M. Toole, and A. J. Watson, 2012: Turbulence and dianeutral mixing in Drake Passage. *J. Phys. Oceanogr.*, **42**, 2143–2152, doi:10.1175/JPO-D-12-027.1.

Taylor, G. I., 1921: Diffusion by continuous movements. *Proc. London Math. Soc.*, **20**, 196–211, doi:10.1112/plms/s2-20.1.196.

Thompson, A. F., and J.-B. Sallée, 2012: Jets and topography: Jet transitions and the impact on transport in the Antarctic Circumpolar Current. *J. Phys. Oceanogr.*, **42**, 956–972, doi:10.1175/JPO-D-11-0135.1.

——, and A. C. Naveira Garabato, 2014: Equilibration of the Antarctic Circumpolar Current by standing meanders. *J. Phys. Oceanogr.*, **44**, 1811–1828, doi:10.1175/JPO-D-13-0163.1.

Visbeck, M., 2002: Deep velocity profiling using lowered acoustic Doppler current profilers: Bottom track and inverse solutions. *J. Atmos. Oceanic Technol.*, **19**, 794–807, doi:10.1175/1520-0426(2002)019<0794:DVPULA>2.0.CO;2.

Waterman, S. N., A. C. Naveira Garabato, and K. L. Polzin, 2013: Internal waves and turbulence in the Antarctic Circumpolar Current. *J. Phys. Oceanogr.*, **43**, 259–282, doi:10.1175/JPO-D-11-0194.1.

Watson, A. J., 2011: Cruise report JR 276 "DIMES UK 2.5": RRS James Clark Ross, 9 April 2011–26 April 2011. British Antarctic Survey, 115 pp. [Available online at https://www.bodc.ac.uk/data/information_and_inventories/cruise_inventory/report/jr276.pdf.]

——, 2012: Cruise report JC 69 "DIMES UK 3": RRS James Cook, 31 January–22 March 2012. British Oceanographic Data Centre, 137 pp. [Available online at https://www.bodc.ac.uk/data/information_and_inventories/cruise_inventory/report/jc069.pdf.]

Wilson, C., and R. G. Williams, 2004: Why are eddy fluxes of potential vorticity difficult to parameterize? *J. Phys. Oceanogr.*, **34**, 142–155, doi:10.1175/1520-0485(2004)034<0142:WAEFOP>2.0.CO;2.

Wunsch, C., 1999: Where do ocean heat fluxes matter? *J. Geophys. Res.*, **104**, 13 235–13 249, doi:10.1029/1999JC900062.

Zika, J. D., B. M. Sloyan, and T. J. McDougall, 2009: Diagnosing the Southern Ocean overturning from tracer fields. *J. Phys. Oceanogr.*, **39**, 2926–2940, doi:10.1175/2009JPO4052.1.

——, T. J. McDougall, and B. M. Sloyan, 2010: A tracer-contour inverse method for estimating ocean circulation and mixing. *J. Phys. Oceanogr.*, **40**, 26–47, doi:10.1175/2009JPO4208.1.